Seamless mapping of long-term (2010-2020) daily global XCO_2 and XCH_4 from GOSAT, OCO-2, and CAMS-EGG4 with a spatiotemporally self-supervised fusion method

Yuan Wang[1], Qiangqiang Yuan[1,2], Tongwen Li[3], Yuanjian Yang[4], Siqin Zhou[1], Liangpei Zhang[5]

[1]School of Geodesy and Geomatics, Wuhan University, Wuhan, Hubei, 430079, China.

[2]The Key Laboratory of Geospace Environment and Geodesy, Ministry of Education, Wuhan University, Wuhan, Hubei, 430079, China.

[3]School of Geospatial Engineering and Science, Sun Yat-sen University, Guangzhou, Guangdong, 519082, China.

[4]School of Atmospheric Physics, Nanjing University of Information Science & Technology, Nanjing, Jiangsu, 210044, China.

[5]The State Key Laboratory of Information Engineering in Surveying, Mapping and Remote Sensing, Wuhan University, Wuhan, Hubei, 430079, China.

Correspondence to: Qiangqiang Yuan (qyuan@sgg.whu.edu.cn)

Abstract. Precise and continuous monitoring on long-term carbon dioxide (CO_2) and methane (CH_4) over the globe is of great importance, which can help study global warming and achieve the goal of carbon neutrality. Nevertheless, the available observations of CO_2 and CH_4 from satellites are generally sparse, and current fusion methods to reconstruct their long-term values on a global scale are few. To address this problem, we propose a novel spatiotemporally self-supervised fusion method to establish long-term daily seamless XCO_2 and XCH_4 products from 2010 to 2020 over the globe at grids of 0.25°. A total of three datasets are applied in our study, including GOSAT, OCO-2, and CAMS-EGG4. Attributed to the significant sparsity of data from GOSAT and OCO-2, the spatiotemporal Discrete Cosine Transform is considered for our fusion task. Validation results show that the proposed method achieves a satisfactory accuracy, with the Standard-Deviation of Bias (σ) of ~ 1.18 ppm for XCO_2 and 11.3 ppb for XCH_4 against TCCON measurements from 2010 to 2020. Meanwhile, the Determination-Coefficient (R^2) of XCO_2 and XCH_4 reach 0.91/0.95 (2010-2014/2015-2020) and 0.9 (2010-2020) after fusion, respectively. Overall, the performance of fused results distinctly exceeds that of CAMS-EGG4, which is also superior or close to those of GOSAT and OCO-2. Especially, our fusion method can effectively correct the large biases in CAMS-EGG4 due to the issues from assimilation data, such as the unadjusted anthropogenic emission inventories for COVID-19 lockdowns in 2020. Moreover, the fused results present coincident spatial patterns with GOSAT and OCO-2, which accurately display the long-term and seasonal changes of globally distributed XCO_2 and XCH_4. The daily global seamless gridded (0.25°) XCO_2 and XCH_4 from 2010 to 2020 can be freely accessed at http://doi.org/10.5281/zenodo.7388893 (Wang et al., 2022b).

1 Introduction

As the most abundant greenhouse gases (GHGs) due to human activities, atmospheric carbon dioxide (CO_2) and methane (CH_4) play significant roles in climate change and directly contribute to global warming (Meinshausen et al., 2009; Montzka et al., 2011; Solomon et al., 2010; Yoro and Daramola, 2020; Shine et al., 2005). For decades, the rising anthropogenic surface emissions of CO_2 and CH_4 result in their long-term rapid uptrends (Choulga et al., 2021; Moran et al., 2022; Lin et al., 2021; Petrescu et al., 2021), which have greatly affected the carbon cycle (Battin et al., 2009; Sjögersten et al., 2014) and ecosystem balance (Liu and Greaver, 2009; Hotchkiss et al., 2015). According to measurements from the Global Greenhouse Gas Reference Network (https://gml.noaa.gov/ccgg/), annual surface CO_2 and CH_4 mole fractions break 412 parts per million (ppm) and 1878 parts per billion (ppb) in 2020, with growths of ~ 68 ppm and 222 ppb since 1985, respectively. To mitigate global warming, the Paris Agreement (https://unfccc.int/process-and-meetings/the-paris-agreement/) has indicated that the increment of temperature should not exceed 2 ℃ (preferably to 1.5 ℃) by comparison with the pre-industrial level. This requires all efforts from the whole society to reach the global peaking of GHGs surface emissions as early as possible, especially for CO_2 and CH_4, which eventually create a carbon-neutral world by mid-century. Therefore, it is an urgent need to precisely and continuously monitor atmospheric CO_2 and CH_4 on a global scale.

To date, remote sensing observations have been extensively adopted in plenty of domains (Wang et al., 2021, 2022c; Zhou et al., 2022), which also emerged as regular techniques to acquire globe-scale atmospheric CO_2 and CH_4 spatial patterns (He et al., 2022a; Buchwitz et al., 2015; Bergamaschi et al., 2013). For instance, the EnviSat can provide global column-mean dry-air mole fraction of CO_2 (XCO_2) and CH_4 (XCH_4) at a coarse resolution of 30×60 km^2, with the payload of the Scanning Imaging Absorption Spectrometer for Atmospheric Cartography (Burrows et al., 1995; Beirle et al., 2018). The Thermal and Near-Infrared Sensor for carbon Observations - Fourier Transform Spectrometer onboard the Greenhouse Gases Observing Satellite (GOSAT) (Hamazaki et al., 2005; Velazco et al., 2019) can produce ~ 10-km XCO_2 and XCH_4 over the globe based on three spectral bands. The Orbiting Carbon Observatory 2/3 (OCO-2/3) (Crisp et al., 2017; Doughty et al., 2022) carries three-channel grating spectrometers to generate globally covered XCO_2 at a much finer spatial resolution of 1.29×2.25 km^2. The Carbon Dioxide Spectrometer named CarbonSpec onboard the TanSat (Liu et al., 2018) of China launched in 2016, which can accurately map high-resolution (~ 2 km) global XCO_2 spatial distribution.

As for long-term observations of XCO_2 and XCH_4, the operational products from GOSAT and OCO-2 are widely applied in carbon-related applications, such as the computation of carbon fluxes (Fraser et al., 2013; Wang et al., 2019), inferring carbon sources and sinks (Deng et al., 2014; Houweling et al., 2015), quantifying CO_2 and CH_4 emissions (Turner et al., 2015; Hakkarainen et al., 2016), and estimation of terrestrial net ecosystem exchange (Jiang et al., 2022). Nevertheless, large-scale missing data consists in the XCO_2 and XCH_4 products from GOSAT and OCO-2, which is attributed to the narrow swath of their observations (Crisp et al., 2017) and contamination of cloud and aerosol (Taylor et al., 2016). Seamless information of

61 XCO_2 and XCH_4 can help better understand the driving factors of long-term variations for CO_2 and CH_4 due to surface

62 emissions and atmospheric transport (Kenea et al., 2023; Liu et al., 2020). In addition, full-coverage XCO_2 and XCH_4 products

63 are more useful to analyze carbon source-sink dynamics (Reithmaier et al., 2021; Crosswell et al., 2017) and impacts on climate

64 changes caused by the elevated CO_2 and CH_4 (Chen et al., 2021; Le Quéré et al., 2019). Hence, it is significant and essential

65 to assure the spatiotemporal continuity of XCO_2 and XCH_4 products from GOSAT and OCO-2, which is conducive to achieving

66 the goal of carbon neutrality.

67 A lot of efforts have been made to generate seamless XCO_2 and XCH_4 products for GOSAT and OCO-2. Initially, interpolation-

68 based methods are widely utilized, such as the fixed rank kriging interpolation (Katzfuss and Cressie, 2011), semantic kriging

69 interpolation (Bhattacharjee et al., 2014), and space-time kriging interpolation (He et al., 2020; Li et al., 2022). However, the

70 interpolated results are usually performed at coarse spatial resolutions (e.g., 1°) and tend to show high uncertainties and over-

71 smoothed distribution due to the extreme sparsity of original data. At present, data fusion techniques (He et al., 2022a, b; Zhang

72 et al., 2022; Zhang and Liu, 2023; Siabi et al., 2019) have emerged as new methods to acquire full-coverage products for

73 GOSAT and OCO-2 at a high spatial resolution, which absorb advantages from multisource data. Generally, these methods

74 exploited machine learning algorithms to train an end-to-end fusion function with multiple seamless data (e.g., model and

75 reanalysis) as inputs. For example, Siabi et al. (2019) employed multi-layer perceptron and eight environmental variables (e.g.,

76 net primary productivity and leaf area index) to map full-coverage XCO_2 in Iran; He et al. (2022b) established seamless results

77 over China using the OCO-2 XCO_2 product, CarbonTracker model data, and auxiliary co-variates based on the light gradient

78 boosting machine; Zhang et al. (2022) proposed a geographically weighted neural network to produce full-coverage XCO_2

79 product across China by fusing the datasets from OCO-2, CAMS-EGG4 (reanalysis), and ERA5; and Zhang and Liu (2023)

80 adopted multiple datasets, e.g., EnviSat, GOSAT, OCO-2, CarbonTracker, and ERA5, and obtained long-term seamless XCO_2

81 product in China through a finely devised neural network.

82 These data fusion approaches provided high-quality results with seamless distribution and greatly enhance the data availability

83 for GOSAT and OCO-2. Nevertheless, the application areas of current fused products merely target at local or national scales,

84 which are insufficient for globe-scale researches. Meanwhile, existing data fusion frameworks are regarded as end-to-end

85 functions, which lack consideration for spatiotemporal self-correlation of original data (e.g., OCO-2). They normally require

86 massive auxiliary co-variates (e.g., ERA5) as inputs and consume a large time in training procedures. Moreover, only XCO_2

87 products are taken into account while the data fusion studies for XCH_4 products are scarce. In conclusion, it is valuable and

88 imperative to generate long-term globally distributed seamless XCO_2 and XCH_4 products for GOSAT and OCO-2 with an

89 efficient data fusion method, which considers the knowledge of their spatiotemporal self-correlation.

90 The present study focuses on generating long-term daily global seamless XCO_2 and XCH_4 products from 2010 to 2020 at the

91 grids of 0.25° via a spatiotemporally self-supervised fusion method. A total of three datasets are utilized in our study without

92 any auxiliary co-variates, including GOSAT, OCO-2, and CAMS-EGG4. CAMS-EGG4 can provide long-term gridded full-

93 coverage XCO_2 and XCH_4 datasets over the globe, which is suitable for our fusion task. Since the data from GOSAT and OCO-

94 2 is significantly sparse in space-time domain (see Fig. 1), the fusion procedures are difficult to be performed. By contrast,

95 frequency domain contains comprehensive information due to its more concentrated signal distribution. Discrete Cosine

96 Transform (DCT) (Rao and Yip, 2014) is an efficient algorithm to convert signal into frequency domain. In this study, a novel

97 self-supervised fusion method based on spatiotemporal DCT (S-STDCT) is developed for the fusion task. Details of the S-

98 STDCT fusion method are presented in Section 3. Validation results show that the S-STDCT fusion method achieves a

99 satisfactory performance. Generally, the accuracy of fused results largely exceeds that of CAMS-EGG4, which is also better

100 than or close to those of GSOAT and OCO-2.
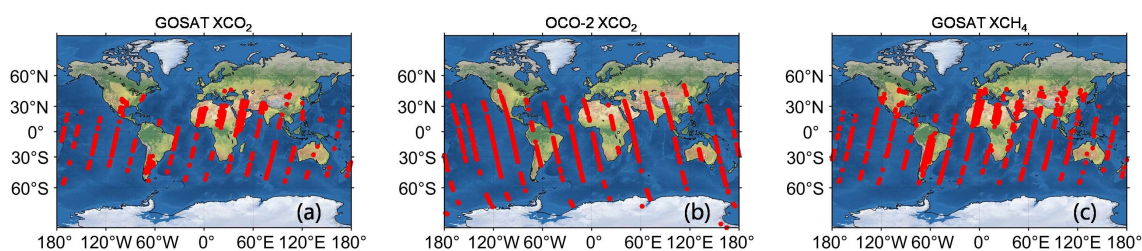
101

102 **Figure 1.** An example of daily spatial footprints for (a) GOSAT XCO_2, (b) OCO-2 XCO_2, and (c) GOSAT XCH_4. Red points signify the

103 available data. Background maps are naturally shaded reliefs over the globe.

104 This paper arranges the remaining sections as follows. Section 2 describes the data records employed in our study, including

105 the XCO_2 and XCH_4 from in-situ stations, GOSAT, and CAMS-EGG4 and XCO_2 from OCO-2. Section 3 provides the

106 specification of the developed S-STDCT fusion method. Section 4 presents the experiment results, which consist of elaborative

107 validations against in-situ measurements and assessments of spatial distribution on multi-temporal scales. At last, conclusions

108 and future works are summarized in section 5.

109 **2 Data description**

110 **2.1 GOSAT XCO_2 and XCH_4 products**

111 A famous XCO_2 retrieval algorithm devised for GOSAT (Taylor et al., 2022), i.e., the Atmospheric CO_2 Observations from

112 Space (ACOS), employs three infrared spectral bands at ~ 0.76, 1.6, and 2.0 μm, which are denoted as Oxygen-A, CO_2 weak,

113 and CO_2 strong, respectively. Regarding XCH_4, the latest retrieval algorithm for GOSAT from the University of Leicester is

114 recently updated, which considers the ratio of XCH_4:XCO_2 as a proxy (Parker et al., 2020). It is based on the theory that the

115 impacts from atmospheric scattering and sensor are mostly similar for XCH_4 and XCO_2 in a shared absorption band at ~ 1.6

116 μm. The GOSAT XCO_2 and XCH_4 products are both performed at spatial resolutions of 10.5 km (diameter) over the globe

117 with revisit times of 3 days. In our study, the scientific data records of "XCO2" in ACOS_L2_Lite_FP (level 2, bias-corrected,

118 V9r) and "XCH4" in UoL-GHG-L2-CH4-GOSAT-OCPR (level 2, V9) are adopted. Furthermore, the quality assurance (QA)

119 records of "XCO2 Quality Flag" and "XCH4 Quality Flag" are exploited to filter bad data. Relevant information of XCO_2 and

120 XCH_4 products from GOSAT is shown in Table 1.

121 **Table 1.** Detailed information of the datasets considered in this study.

Source	Scientific data record	Version	Spatial resolution	Temporal resolution	Period
GOSAT	XCO2 XCO2 Quality Flag XCH4 XCH4 Quality Flag	V9r V9	10.5 km (diameter)	Daily (~ 13:00 local time)	2010-2014 2010-2020
OCO-2	XCO2 XCO2 Quality Flag XCO2 XCO2 Quality Flag	V10r V11r	1.29×2.25 km^2	Daily (~ 13:36 local time)	2015-2017 2018-2020
CAMS-EGG4	CO2 column-mean molar fraction CH4 column-mean molar fraction	-	0.75°	3 hours	2010-2020

122 **2.2 OCO-2 XCO_2 product**

123 Apart from GOSAT, the ACOS XCO_2 retrieval algorithm is also applied to OCO-2 observations (Kiel et al., 2019), which

124 utilizes the same bands of the Oxygen-A, CO_2 weak, and CO_2 strong. OCO-2 provides a global XCO_2 product at a high spatial

125 resolution of 1.29×2.25 km^2 with a revisit time of 16 days. After 2015, the XCO_2 product from OCO-2 is used for fusion

126 instead of GOSAT due to its more observation counts and better accuracy. In this study, the scientific data record of "XCO2"

127 in OCO2_L2_Lite_FP (level 2, bias-corrected) is applied in the fusion with CAMS-EGG4 using the developed method.

128 Moreover, the QA record of "XCO2 Quality Flag" is adopted to filter bad data. Since the OCO-2 XCO_2 product of the latest

129 version (V11r) is still on processing, both data of V10r and V11r are considered in our study. Related information of XCO_2

130 product from OCO-2 is given in Table 1.

131 **2.3 CAMS-EGG4 GHGs reanalysis datasets**

132 CAMS-EGG4 is recent globally distributed operational GHGs reanalysis datasets supported by the European Centre for

133 Medium-range Weather Forecasts (Agusti-Panareda et al., 2022). It assimilates the forecasts from the Integrated Forecasting

134 System with multiple satellite products, which include Envisat, GOSAT, and Metop-A/B (August et al., 2012), via physical

135 and chemistry principles. The CAMS-EGG4 can generate long-term gridded seamless XCO_2 and XCH_4 datasets and related

136 fields at spatial and temporal resolutions of 0.75° and 3 hours, respectively. Unfortunately, there are a few limitations in CAMS-

137 EGG4, such as the uncorrected anthropogenic emissions for COronaVIrus Disease 2019 (COVID-19) lockdowns, which are

138 scheduled to be fixed by the official team in the future (Agusti-Panareda et al., 2022). It is worth noting that the XCO_2 and

139 XCH_4 products from GOSAT and OCO-2 employed in this paper are not assimilated in CAMS-EGG4. In our study, the

140 scientific data records of "CO2 column-mean molar fraction" and "CH4 column-mean molar fraction" are exploited for the

141 fusion with GOSAT and OCO-2 through the developed method. Details of CAMS-EGG4 datasets are provided in Table 1.

2.4 TCCON measurements

In our study, the XCO_2 and XCH_4 measurements provided by an international in-situ network, which is named after TCCON (Wunch et al., 2011) (https://tccondata.org/), are utilized to validate the fused results. The in-situ measurements of TCCON are extensively used in the validation for XCO_2 and XCH_4 products from GOSAT, OCO-2, and CAMS-EGG4 (Hong et al., 2022; Yoshida et al., 2013; Wunch et al., 2017; Wu et al., 2018; Agusti-Panareda et al., 2022). Figure 2 depicts the spatial locations of TCCON stations, with the marks of white-edged red circles. The measurements of version GGG2020 (Laughner et al., 2022) from 29 stations around the world are adopted. Specific information of the stations is listed in Table 2.
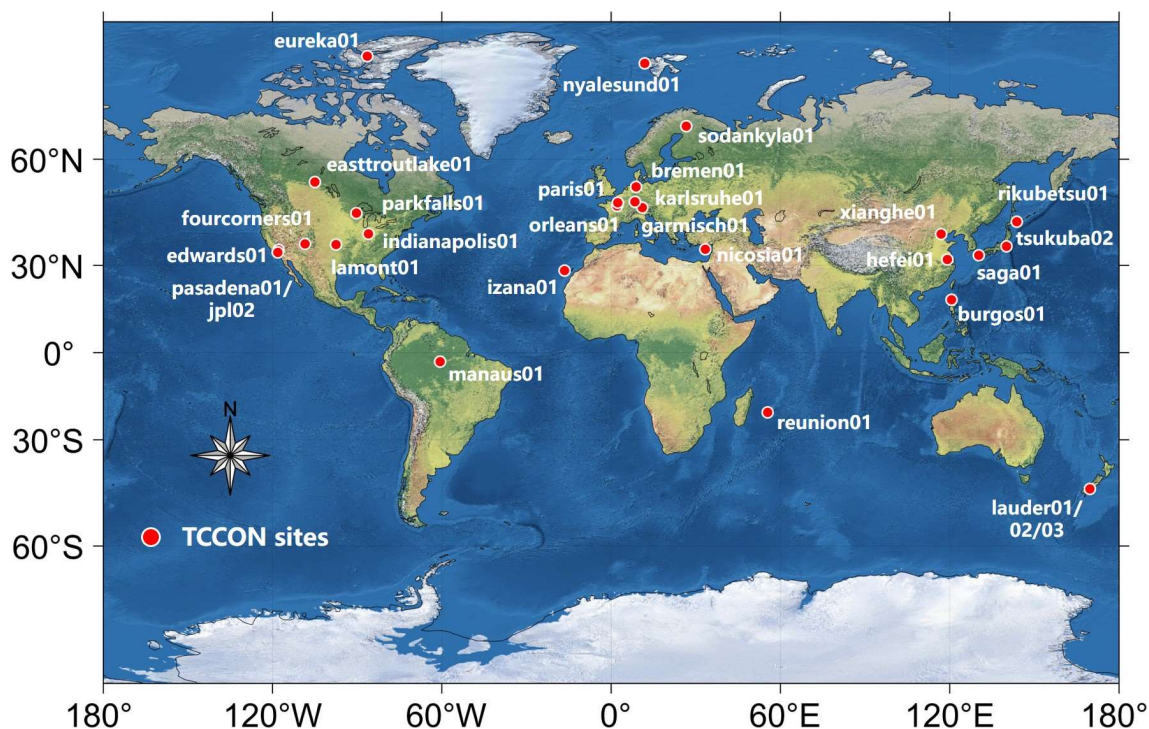
Figure 2. Spatial locations of in-situ stations from TCCON used in the present study. The background map is a naturally shaded relief over the globe.

3 Methodology

3.1 Data pre-processing

Data pre-processing is an important procedure to ensure the rationality and reliability of fused results. In this study, the values of "QA=0" in XCO_2 and XCH_4 from GOSAT and OCO-2 are discarded, which filters the bad data. Besides, the CAMS-EGG4 XCO_2 and XCH_4 at a temporal resolution of 3 hours are averaged in a single day to produce daily datasets. Finally, the spatial resolutions of XCO_2 and XCH_4 from GOSAT, OCO-2, and CAMS-EGG4 ought to be adjusted to the same value. A globally covered grid of 721×1441 (0.25º) is employed in our study. The XCO_2 and XCH_4 from GOSAT, OCO-2, and CAMS-EGG4 are re-gridded to 0.25° using the area-weighted aggregation (Wang et al., 2021) and Inverse Distance Weighted (Mueller et al., 2004) interpolation, respectively.

Table 2. Detailed information of TCCON in-situ stations adopted in our study. No.: number.

No.	Site name	Latitude	Longitude	Location	Start date	End date
1	bremen01	53.10	8.85	Europe	2010-01-01	2020-12-31
2	burgos01	18.53	120.65	Asia	2017-03-03	2020-04-30
3	easttroutlake01	54.36	-104.99	North America	2016-10-03	2020-12-31
4	edwards01	34.96	-117.88	North America	2013-07-20	2020-12-31
5	eureka01	80.05	-86.42	North America	2010-07-24	2020-07-07
6	fourcorners01	36.80	-108.48	North America	2013-03-16	2013-10-03
7	garmisch01	47.48	11.06	Europe	2010-01-01	2020-12-31
8	hefei01	31.90	119.17	Asia	2016-01-08	2020-12-31
9	indianapolis01	39.86	-86.00	North America	2012-08-23	2012-12-01
10	izana01	28.31	-16.50	Atlantic Ocean	2014-01-02	2020-12-31
11	jpl02	34.20	-118.18	North America	2011-05-19	2018-05-14
12	karlsruhe01	49.10	8.44	Europe	2014-01-15	2020-12-31
13	lauder01	36.60	-97.49	Oceania	2010-01-01	2010-02-19
14	lauder02	-45.04	169.68	Oceania	2013-01-02	2018-09-30
15	lauder03	-45.04	169.68	Oceania	2018-10-02	2020-12-31
16	lamont01	-45.04	169.68	North America	2010-01-01	2020-12-31
17	manaus01	-3.21	-60.60	South America	2014-09-30	2015-07-27
18	nicosia01	35.14	33.38	Asia	2019-09-03	2020-12-31
19	nyalesund01	78.92	11.92	Arctic Ocean	2010-01-01	2020-12-31
20	orleans01	47.96	2.11	Europe	2010-01-01	2020-12-31
21	paris01	48.85	2.36	Europe	2014-09-23	2020-12-31
22	parkfalls01	45.94	-90.27	North America	2010-01-01	2020-12-31
23	pasadena01	34.14	-118.13	North America	2012-09-20	2020-12-31
24	reunion01	-20.90	55.48	Indian Ocean	2015-03-01	2020-07-18
25	rikubetsu01	43.46	143.77	Asia	2014-06-24	2020-12-31
26	saga01	33.24	130.29	Asia	2011-07-28	2020-12-31
27	sodankyla01	67.37	26.63	Europe	2018-03-05	2020-12-31
28	tsukuba02	36.05	140.12	Asia	2014-03-28	2020-12-31
29	xianghe01	39.80	116.96	Asia	2018-06-14	2020-12-31

3.2 Spatiotemporally self-supervised fusion method

Since the sparsity of data from GOSAT and OCO-2 is significant in space-time domain (see Fig. 1), it is difficult to perform fusion procedures for them. In contrast, frequency domain is more suitable because of its concentrated signal distribution. DCT is an efficient algorithm to transform signal into frequency domain (Rao and Yip, 2014), which has been widely applied in image compression (Cintra and Bayer, 2011), geophysical data filtering (El-Mahallawy and Hashim, 2013), and remote sensing data reconstruction (Wang et al., 2012, 2022a; Fredj et al., 2016; Pham et al., 2019). In our study, a novel self-supervised fusion method based on spatiotemporal DCT, i.e., S-STDCT, is developed for the fusion task, which fully adopts the spatiotemporal knowledge of self-correlation in GOSAT and OCO-2 products.

3.2.1 Spatiotemporal DCT

A total of eight types of DCT are proposed, among which the second type (type-II) is commonly utilized due to its simple calculation and broad application range (Rao and Yip, 2014). Hence, the type-II DCT is considered in this study. The spatiotemporal DCT is a 3-dimensional form (hereafter *STDCT*), which can be expressed as Eq. (1):

$$174 \quad X(u,v,w) = c(u)c(v)c(w) \sum_{i=0}^{M-1} \sum_{j=0}^{N-1} \sum_{t=0}^{P-1} x(i,j,t) cos\left[\frac{(i+0.5)\pi}{M}u\right] cos\left[\frac{(j+0.5)\pi}{N}v\right] cos\left[\frac{(t+0.5)\pi}{P}w\right], \quad (1)$$

175   where $c(u) = \begin{cases} \sqrt{\frac{1}{M}}, u=0 \\ \sqrt{\frac{2}{M}}, u \neq 0 \end{cases}$, $c(v) = \begin{cases} \sqrt{\frac{1}{N}}, v=0 \\ \sqrt{\frac{2}{N}}, v \neq 0 \end{cases}$, $c(w) = \begin{cases} \sqrt{\frac{1}{P}}, w=0 \\ \sqrt{\frac{2}{P}}, w \neq 0 \end{cases}$; x indicates the original 3-dimensional tensor; M, N,

176   and P stand for the counts of rows (latitude), columns (longitude), and temporal sequences (days), which equal 721 (0.25°,

177   global grids), 1441 (0.25°, global grids), and days of a year (365 or 366), respectively; i, j, and t represent the row, column,

178   and temporal sequence, respectively ($i \in [0, M\text{-}1], j \in [0, N\text{-}1]$, and $t \in [0, P\text{-}1]$); X signifies the transformed 3-dimensional

179   tensor; u, v, and w denote the transformed coordinates in frequency domain, which share the same ranges with i, j, and t (e.g.,

180    $u \in [0, M\text{-}1]$), respectively. The inverse transformation of *STDCT* (hereafter *ISTDCT*) is provided in Eq. (2):

$$181 \quad x(i,j,t) = c(u)c(v)c(w) \sum_{u=0}^{M-1} \sum_{v=0}^{N-1} \sum_{w=0}^{P-1} X(u,v,w) cos\left[\frac{(i+0.5)\pi}{M}u\right] cos\left[\frac{(j+0.5)\pi}{N}v\right] cos\left[\frac{(t+0.5)\pi}{P}w\right], \quad (2)$$

182   **3.2.2 Self-supervised fusion scheme with spatiotemporal knowledge**

183   It has been documented that the XCO_2 and XCH_4 products derived from remote sensing satellites generally present better

184   accuracy compared to reanalysis datasets (Agusti-Panareda et al., 2022; He et al., 2022a; Parker et al., 2020). Therefore, the

185   brand new XCO_2 and XCH_4 products from GOSAT and OCO-2 are regarded as the criteria (or ground truths), which will be

186   fused with CAMS-EGG4 datasets. At first, a spatially and temporally varying function relationship (see Eq. (3)) is

187   hypothesized between GOSAT/OCO-2 and CAMS-EGG4 XCO_2/XCH_4 values.

188    $XG_s = f(XGc, Row, Col, Time),$ (3)

189   where XG_s denotes the XCO_2/XCH_4 values from GOSAT/OCO-2; XG_c indicates the XCO_2/XCH_4 values from CAMS-EGG4;

190   *Row*, *Col*, and *Time* represent the row (or latitude), column (or longitude), and temporal sequence, respectively. To conveniently

191   solve this problem, Eq. (3) is simplified into the scalar product form of XG_c and a spatially and temporally varying tensor

192   (defined as δ), as shown in Eq. (4):

193    $XG_s = XGc * \delta(Row, Col, Time),$ (4)

194   Afterward, the factor (i.e., δ) can be acquired using the XCO_2/XCH_4 values at the grids where the GOSAT/OCO-2 and CAMS-

195   EGG4 data are both available. In our study, a self-supervised fusion scheme is introduced to solve Eq. (4) based on the

196   spatiotemporal knowledge of self-correlation in GOSAT and OCO-2 products. Due to the large sparsity of data from GOSAT

197   and OCO-2 in space-time domain, the *STDCT* is applied for the fusion task.

198   Inspired by previous studies adopting the *STDCT* (Garcia, 2010; Wang et al., 2012, 2022a; Fredj et al., 2016; Pham et al.,

199   2019), the S-STDCT fusion method searches for the spatially and temporally varying tensor, i.e., $\hat{\delta}$, that minimizes Eq. (5),

200   including a residual (left) and a smoothing (right) term.

201 $\quad E(\hat{\delta}) = \left\| \varphi^{\frac{1}{2}} * (\hat{\delta} - \delta) \right\|^2 + \varepsilon \| \nabla^2 \hat{\delta} \|^2,$ (5)

202 where $\| \: \|$ signifies the Euclidean norm; φ represents the binary mask showing the data is whether available or not; ε and

203 ∇^2 indicate a smoothing factor and the Laplace operator, respectively. This equation can be solved by iterations via Eq. (6):

204 $\quad \hat{\delta} = \gamma ISTDCT \left(\rho * STDCT \left(\varphi * \left(\delta - \hat{\delta} \right) + \hat{\delta} \right) \right) + (1 - \gamma)\hat{\delta},$ (6)

205 where γ is a relaxation factor to accelerate convergence; ρ indicates a 3-dimensional filter related to the smoothing term,

206 which is defined in Eq. (7):

207 $\quad \rho(d_1, d_2, d_3) = \dfrac{1}{1 + \varepsilon \sum_{k=1}^{3} 2 \left[1 - \cos \dfrac{(d_k - 1)\pi}{n_k} \right]},$ (7)

208 Here, d_k represents the dth value along the kth dimension (k = 1, 2, and 3); n_k denotes the size of δ along the kth dimension.

209 Namely, d_1, d_2, and d_3 stand for u, v, and w (see Eq. (1)), respectively. In this study, the number of total iterations, γ, and

210 ε are empirically configured to 100, 1.5, and a range from 10^3 to 10^{-1} (spaced with 100 intervals), respectively. It is worth

211 noting that $\hat{\delta}$ is initialized through the spatiotemporal nearest neighbor interpolation. More details about the solution steps

212 can be found in Garcia (2010).

213
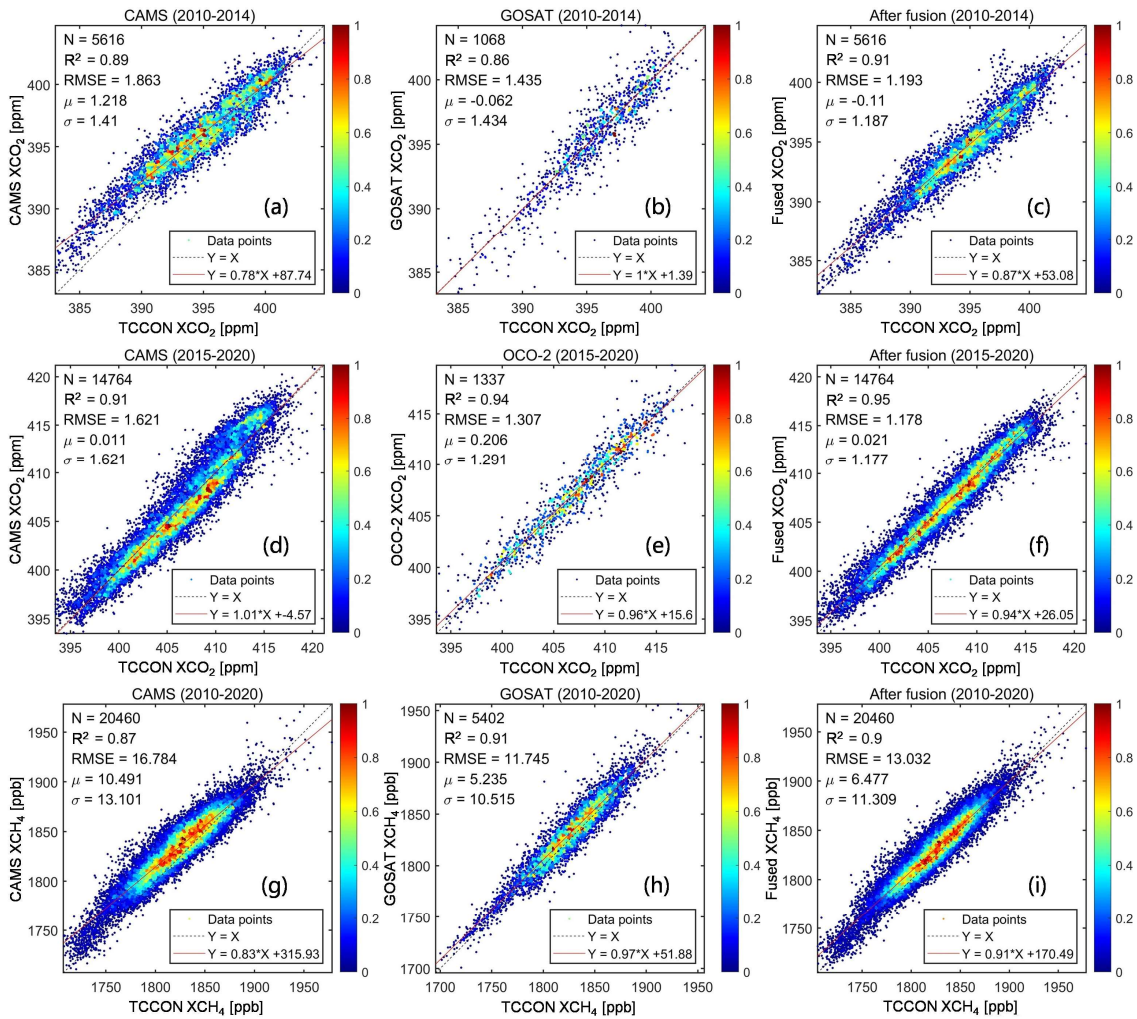
214 **Figure 3.** Density scatter-plots of the in-situ validation results for (a, d, and g) CAMS-EGG4, (b and h) GOSAT, (e) OCO-2, and (c, f, and

215 i) fused results. Black dotted and red full lines stand for the 1:1 and fitted lines, respectively. Color ramps show the normalized densities of

216 data points. X: TCCON data; Y: CAMS-EGG4/GOSAT/OCO-2/fused data. Unit: ppm/ppb to XCO$_2$/XCH$_4$ for RMSE, μ, and σ.

3.3 Evaluation schemes

In our study, the evaluation schemes include in-situ validations and assessments of spatial distribution. To be specific, the GOSAT, OCO-2, CAMS-EGG4, and fused XCO_2 and XCH_4 are validated against TCCON measurements, which consists of the comparisons for overall and individual in-situ stations. The spatial distribution of the GOSAT, OCO-2, CAMS-EGG4, and fused XCO_2 and XCH_4 are assessed on multi-temporal scales, i.e., multi-year mean, seasonal, and annual. A total of four metrics are exploited, covering the Determination-Coefficient (R^2), Root-Mean-Square-Error (RMSE), Mean-Bias (μ), and Standard-Deviation of Bias (σ). The significance levels of $p < 0.01$ are applied in the computations of all metrics.
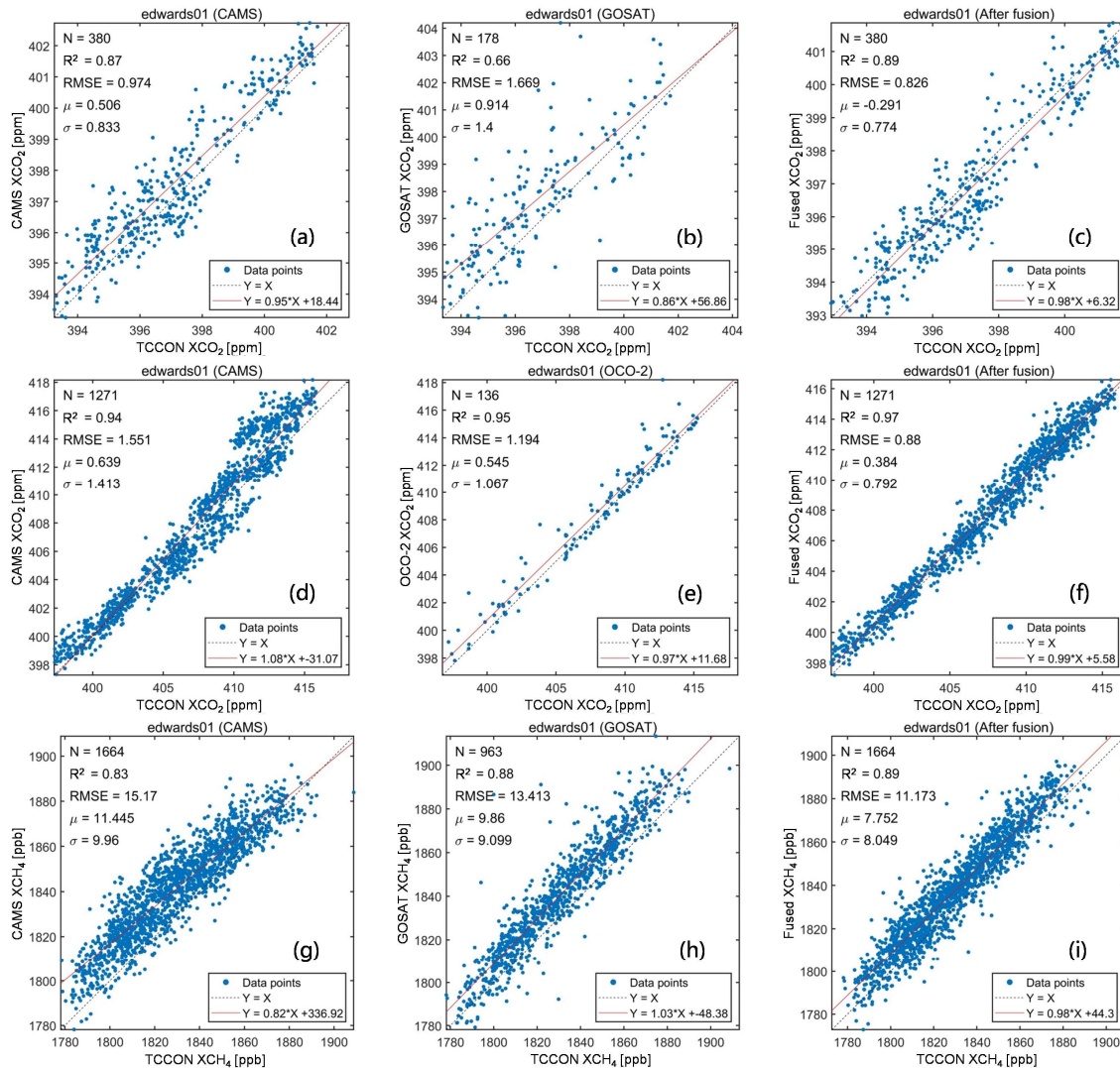
Figure 4. Scatter-plots of the in-situ validation results for (a, d, and g) CAMS-EGG4, (b and h) GOSAT, (e) OCO-2, and (c, f, and i) fused results on edwards01. Black dotted and red full lines stand for the 1:1 and fitted lines, respectively. X: TCCON data; Y: CAMS-EGG4/GOSAT/OCO-2/fused data. Unit: ppm/ppb to XCO_2/XCH_4 for RMSE, μ, and σ.

4 Experiment results and discussions

4.1 Overall in-situ validation

As displayed in Fig. 2, the XCO_2 and XCH_4 measurements from 29 TCCON in-situ stations are adopted for the validation, which evenly distribute over the globe. In this study, TCCON measurements of ± 1 hour on the satellite overpass times (~

232 13:00 and 13:36 local time, see Table 2) are co-matched with the CAMS-EGG4/GOSAT/OCO-2/fused data around each station

233 with a diameter of 2°. Figure 3 depicts the overall in-situ validation results for the CAMS-EGG4, GOSAT, OCO-2, and fused

234 results. The amounts of data points (N) are sufficient (e.g., 1337 for OCO-2 XCO_2 and 5402 for GOSAT XCH_4) to support the

235 reliability of validation results.

236
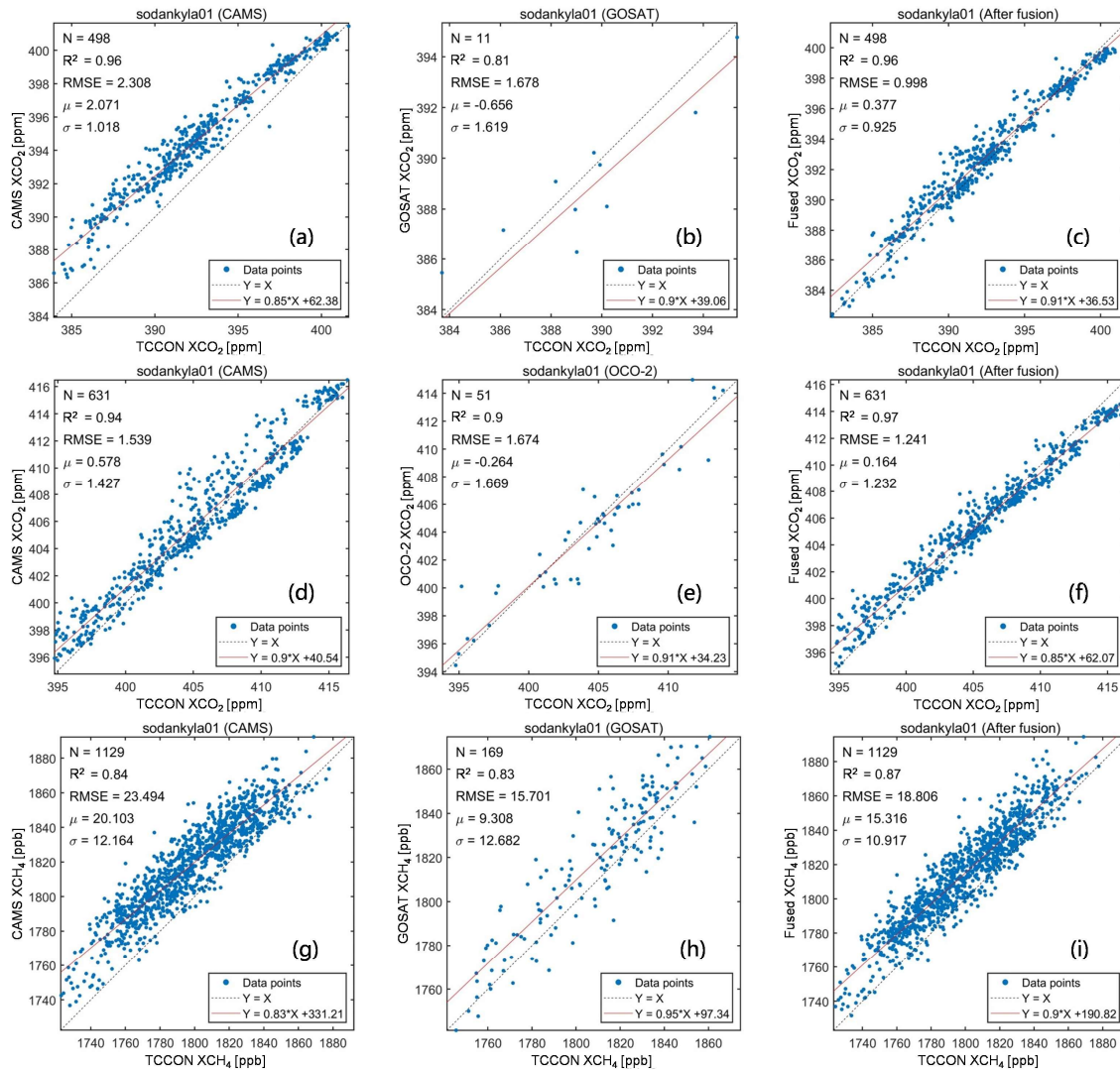
237 **Figure 5.** Scatter-plots of the in-situ validation results for (a, d, and g) CAMS-EGG4, (b and h) GOSAT, (e) OCO-2, and (c, f, and i) fused

238 results on sodankyla01. Black dotted and red full lines stand for the 1:1 and fitted lines, respectively. X: TCCON data; Y: CAMS-

239 EGG4/GOSAT/OCO-2/fused data. Unit: ppm/ppb to XCO_2/XCH_4 for RMSE, μ, and σ.

240 As shown in Fig. 3, the XCO_2 from OCO-2 and XCH_4 from GOSAT perform better than those from CAMS-EGG4, with larger

241 R^2, smaller RMSE, and smaller σ. After fusion, the XCO_2 (2015-2020) and XCH_4 (2010-2020) present a greatly superior

242 accuracy compared to CAMS-EGG4, of which the RMSE (σ) improvements are 0.443 (0.444) ppm and 3.752 (1.792) ppb for

243 XCO_2 and XCH_4, respectively. Meanwhile, the accuracy of the fused results is higher than and close to those of OCO-2 XCO_2

244 and GOSAT XCH_4, respectively. These suggest that the proposed fusion method achieves a satisfactory result. Furthermore,

245 the performance of XCO_2 from GOSAT is similar to that of CAMS-EGG4. However, the fused XCO_2 (2010-2014) shows

246 higher accuracy by comparison with both CAMS-EGG4 and GOSAT, indicating the spatiotemporally local fusion ability of S-

247 STDCT. In conclusion, our fusion method can successfully fuse the data from CAMS-EGG4 and satellites, which effectively

  generates GOSAT-like and OCO-2-like values.

249 **Table 3.** Metrics of the individual in-situ validation results for CAMS-EGG4, GOSAT, and fused XCO$_2$. The best and second metrics are
250 denoted with bold and underlined fonts. CAMS: CAMS-EGG4; AF: after fusion. Unit: ppm for RMSE and σ.

Site name	R^2			RMSE			σ		
	CAMS	GOSAT	AF	CAMS	GOSAT	AF	CAMS	GOSAT	AF
bremen01	0.91	0.85	**0.92**	2.810	1.732	**1.533**	1.376	1.757	**1.189**
edwards01	0.87	0.66	**0.89**	0.974	1.669	**0.826**	0.833	1.400	**0.774**
fourcorners01	0.88	**0.91**	0.86	1.237	0.867	**0.844**	0.848	**0.590**	0.801
garmisch01	0.91	0.86	**0.93**	2.141	1.575	**1.070**	1.275	1.592	**1.067**
jpl02	0.89	0.86	**0.90**	1.535	1.299	**1.075**	0.961	1.299	**0.918**
saga01	0.90	0.91	**0.93**	1.362	1.494	**1.333**	1.313	1.201	**1.065**
lauder02	0.83	0.70	**0.87**	**0.584**	1.095	0.606	**0.585**	1.088	0.600
lamont01	0.79	**0.88**	**0.88**	1.928	0.986	**0.976**	1.327	**0.973**	0.976
orleans01	0.89	0.75	**0.91**	2.105	1.666	**0.964**	1.144	1.440	**0.964**
parkfalls01	0.92	0.86	**0.93**	2.088	1.703	**1.138**	1.309	1.697	**1.137**
pasadena01	0.70	0.74	**0.75**	**1.260**	1.296	1.642	1.261	1.287	**1.177**
sodankyla01	**0.96**	0.81	**0.96**	2.308	1.678	**0.998**	1.018	1.619	**0.925**
tsukuba02	0.80	**0.82**	0.78	**1.179**	1.651	1.494	**1.157**	1.263	1.202

251 **Table 4.** Metrics of the individual in-situ validation results for CAMS-EGG4, OCO-2, and fused XCO$_2$. The best and second metrics are
252 denoted with bold and underlined fonts. CAMS: CAMS-EGG4; AF: after fusion. Unit: ppm for RMSE and σ.

Site name	R^2			RMSE			σ		
	CAMS	OCO-2	AF	CAMS	OCO-2	AF	CAMS	OCO-2	AF
bremen01	0.91	**0.99**	0.93	1.718	**1.126**	1.476	1.678	**1.066**	1.459
burgos01	0.91	**0.95**	0.94	1.324	**0.715**	0.933	1.144	**0.709**	0.823
edwards01	0.94	0.95	**0.97**	1.551	1.194	**0.880**	1.413	1.067	**0.792**
easttroutlake01	0.92	0.87	**0.94**	1.334	1.802	**1.195**	1.303	1.812	**1.196**
eureka01	0.94	0.93	**0.97**	2.081	2.224	**1.427**	1.436	1.555	**1.171**
garmisch01	0.91	0.93	**0.96**	1.586	1.569	**1.019**	1.579	1.354	**1.010**
hefei01	0.88	**0.97**	0.91	1.447	**1.163**	1.283	1.450	**0.735**	1.192
izana01	0.96	0.88	**0.99**	1.215	1.413	**0.576**	1.209	1.417	**0.555**
jpl02	0.75	**0.89**	0.76	2.151	**1.146**	1.525	1.221	**0.885**	1.174
saga01	0.89	**0.95**	0.94	1.890	**1.087**	1.263	1.873	**1.090**	1.254
karlsruhe01	0.89	**0.93**	**0.93**	1.747	**1.327**	1.375	1.749	**1.318**	1.376
lauder02	0.96	0.89	**0.97**	1.213	1.000	**0.492**	0.518	0.993	**0.469**
lauder03	**0.94**	0.72	**0.94**	1.288	1.064	**0.565**	0.863	1.070	**0.538**
nicosia01	0.79	0.91	**0.94**	2.319	**0.731**	0.862	1.133	0.661	**0.641**
nyalesund01	0.94	0.93	**0.97**	1.942	2.233	**1.664**	1.573	1.707	**1.446**
lamont01	0.92	**0.97**	0.96	1.505	**0.956**	0.964	1.489	**0.794**	0.929
orleans01	0.92	0.93	**0.96**	1.450	1.144	**1.108**	1.361	1.121	**1.007**
parkfalls01	0.93	**0.96**	0.95	1.518	1.210	**1.160**	1.518	1.211	**1.160**
pasadena01	0.91	0.93	**0.95**	1.689	1.543	**1.382**	1.581	1.329	**1.160**
paris01	0.89	0.92	**0.93**	1.910	**1.418**	1.451	1.867	**1.433**	1.437
reunion01	0.96	**0.97**	**0.97**	1.276	0.878	**0.874**	0.827	0.886	**0.812**
rikubetsu01	0.90	**0.96**	0.93	1.688	**1.023**	1.320	1.667	**1.033**	1.293
sodankyla01	0.94	0.90	**0.97**	1.539	1.674	**1.241**	1.427	1.669	**1.232**
tsukuba02	0.92	**0.94**	0.93	1.429	**1.169**	1.276	1.322	**1.134**	1.265
xianghe01	0.61	**0.89**	0.73	2.513	**1.411**	1.960	2.487	**1.430**	1.959

253

254 **Table 5.** Metrics of the individual in-situ validation results for CAMS-EGG4, GOSAT, and fused XCH4. The best and second metrics are
255 denoted with bold and underlined fonts. CAMS: CAMS-EGG4; AF: after fusion. Unit: ppb for RMSE and σ.

Site name	R^2			RMSE			σ		
	CAMS	GOSAT	AF	CAMS	GOSAT	AF	CAMS	GOSAT	AF
bremen01	0.84	**0.90**	0.87	19.397	15.328	**14.969**	12.507	**9.868**	10.938
burgos01	0.80	**0.89**	0.89	10.981	10.455	**8.096**	9.194	**6.136**	7.216
edwards01	0.83	0.88	**0.89**	15.170	13.413	**11.173**	9.960	9.099	**8.049**
fourcorners01	0.40	**0.71**	0.51	14.732	**7.714**	9.847	9.711	**6.710**	8.777
garmisch01	0.83	0.85	**0.89**	16.693	13.258	**12.267**	11.568	11.643	**9.577**
hefei01	0.54	0.56	**0.66**	22.072	**15.377**	16.814	16.165	**13.370**	13.826
jpl02	0.81	**0.88**	0.86	16.989	**9.679**	9.788	11.288	**8.840**	9.604
saga01	0.85	**0.92**	0.89	11.299	**9.089**	9.311	10.091	**8.422**	9.147
karlsruhe01	0.70	0.80	**0.81**	13.688	11.913	**10.042**	11.564	11.370	**9.177**
lauder02	0.66	**0.84**	0.65	18.460	**8.632**	11.323	11.390	**6.923**	10.189
lauder03	0.46	**0.76**	0.57	16.568	**8.531**	12.166	10.965	**6.491**	9.347
lamont01	0.82	**0.94**	0.88	11.762	12.204	**9.497**	11.494	**7.015**	9.460
orleans01	0.80	**0.88**	0.88	18.341	13.734	**13.305**	12.038	9.690	**9.395**
parkfalls01	0.79	**0.87**	0.84	17.107	14.892	**13.784**	13.396	**10.548**	11.519
pasadena01	0.82	**0.90**	0.88	12.658	**8.396**	8.845	10.544	8.094	**8.802**
paris01	0.75	0.73	**0.84**	12.313	13.077	**9.578**	10.319	11.437	**8.383**
reunion01	0.51	0.41	**0.73**	18.245	13.846	**10.092**	10.221	11.427	**7.432**
rikubetsu01	0.60	**0.81**	0.72	21.166	20.160	**18.250**	15.263	**11.481**	12.759
sodankyla01	0.84	0.83	**0.87**	23.494	**15.701**	18.806	12.164	12.682	**10.917**
tsukuba02	0.77	**0.86**	0.83	11.726	**8.165**	8.704	9.401	**7.623**	8.424
xianghe01	0.63	**0.69**	0.63	**14.851**	15.840	15.266	**14.734**	13.752	14.736
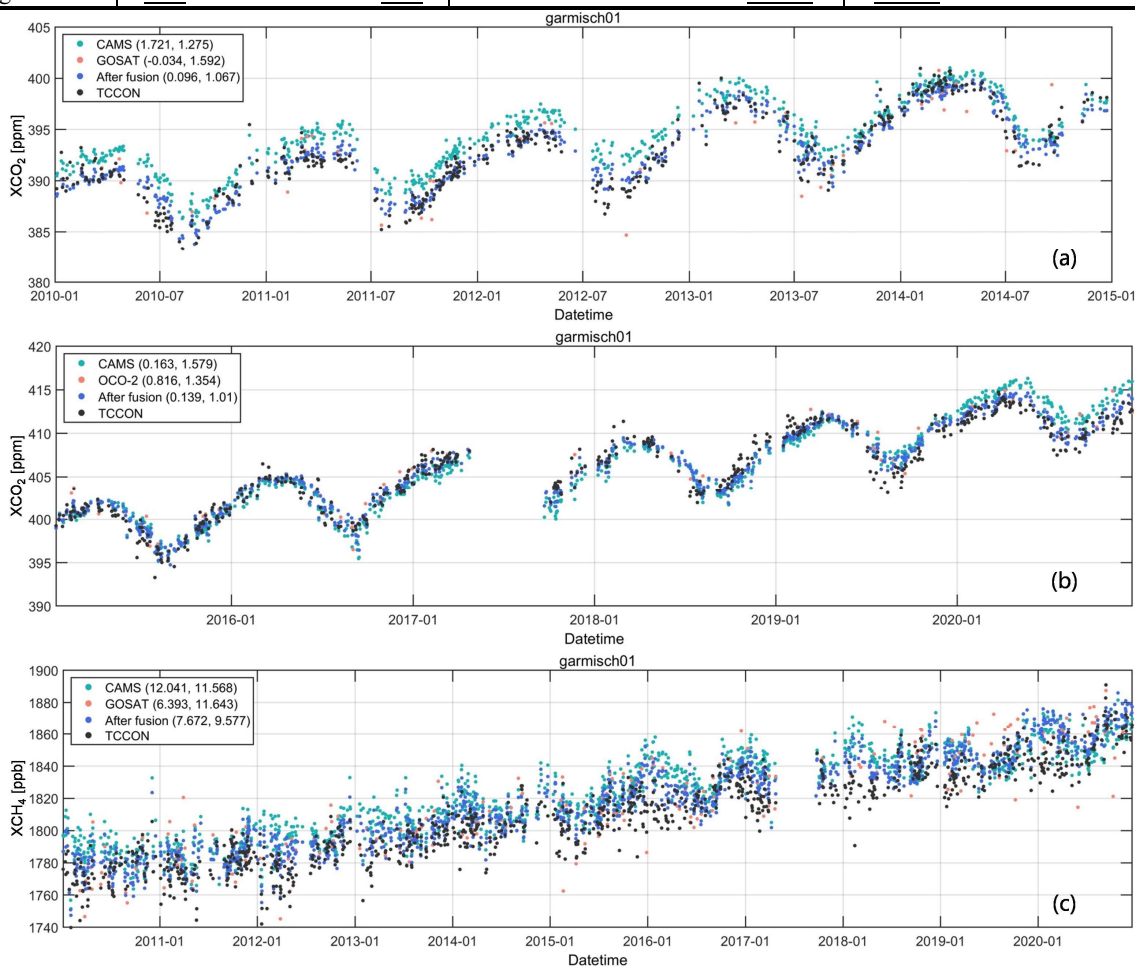
256
257 **Figure 6.** Scatter-plots of the time series for daily CAMS-EGG4, GOSAT, OCO-2, fused, and TCCON data on garmisch01. The first and
258 second numbers in the bracket represent μ and σ, respectively. Unit: ppm/ppb to XCO2/XCH4 for μ and σ.

4.2 Individual in-situ validation and time series

Figure 4, 5, and Table 3-5 show the individual in-situ validation results for the CAMS-EGG4, GOSAT, OCO-2, and fused results on each TCCON in-situ station. It is worth noting that only the stations where the individual validation results are significant (p-level < 0.01) for all datasets (i.e., CAMS-EGG4, GOSAT, OCO-2, and the fused results) are presented. Since the space of text is limited, two stations named edwards01 and sodankyla01 are selected as examples (see Fig. 4 and 5), which locate in North America and Europe, respectively. As can be seen, the fused results achieve the best performance compared to CAMS-EGG4, GOSAT, and OCO-2 on edwards01 and sodankyla01, with the R^2 ranging from 0.87 to 0.97. Especially, the large overestimation of XCO_2 for CAMS-EGG4 on sodankyla01 (μ = 2.071 ppm) is well mitigated after fusion (μ = 0.377 ppm), even for the poor data availability of GOSAT (N = 11). This indicates the strong universality of the proposed fusion method. The valid individual validation results on all stations are given in Table 3-5. It can be observed that the performance of the fused results exceeds those of CAMS-EGG4 and GOSAT/OCO-2 for almost all stations and ~ 70 % of stations, respectively.
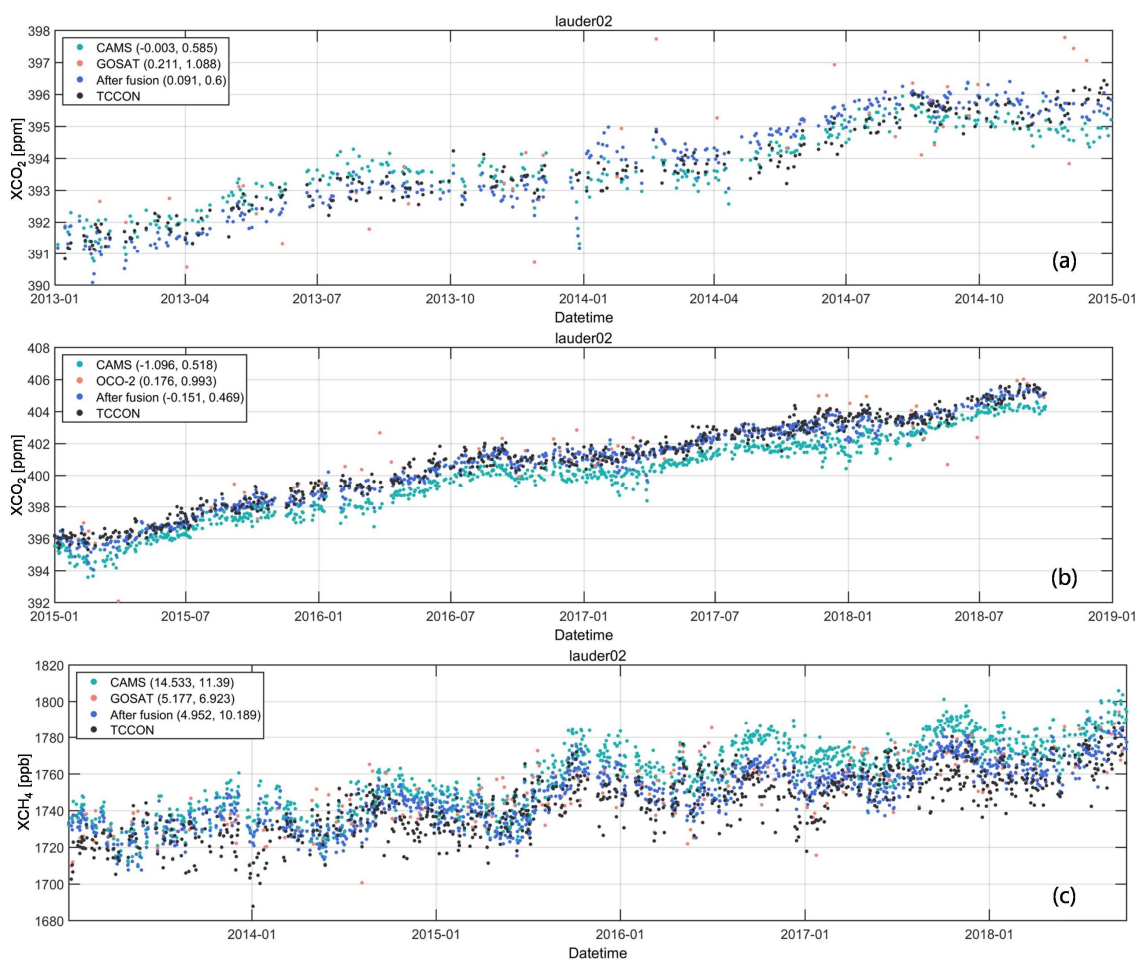
Figure 7. Scatter-plots of the time series for daily CAMS-EGG4, GOSAT, OCO-2, fused, and TCCON data on lauder02. The first and second numbers in the bracket represent μ and σ, respectively. Unit: ppm/ppb to XCO_2/XCH_4 for μ and σ.

274
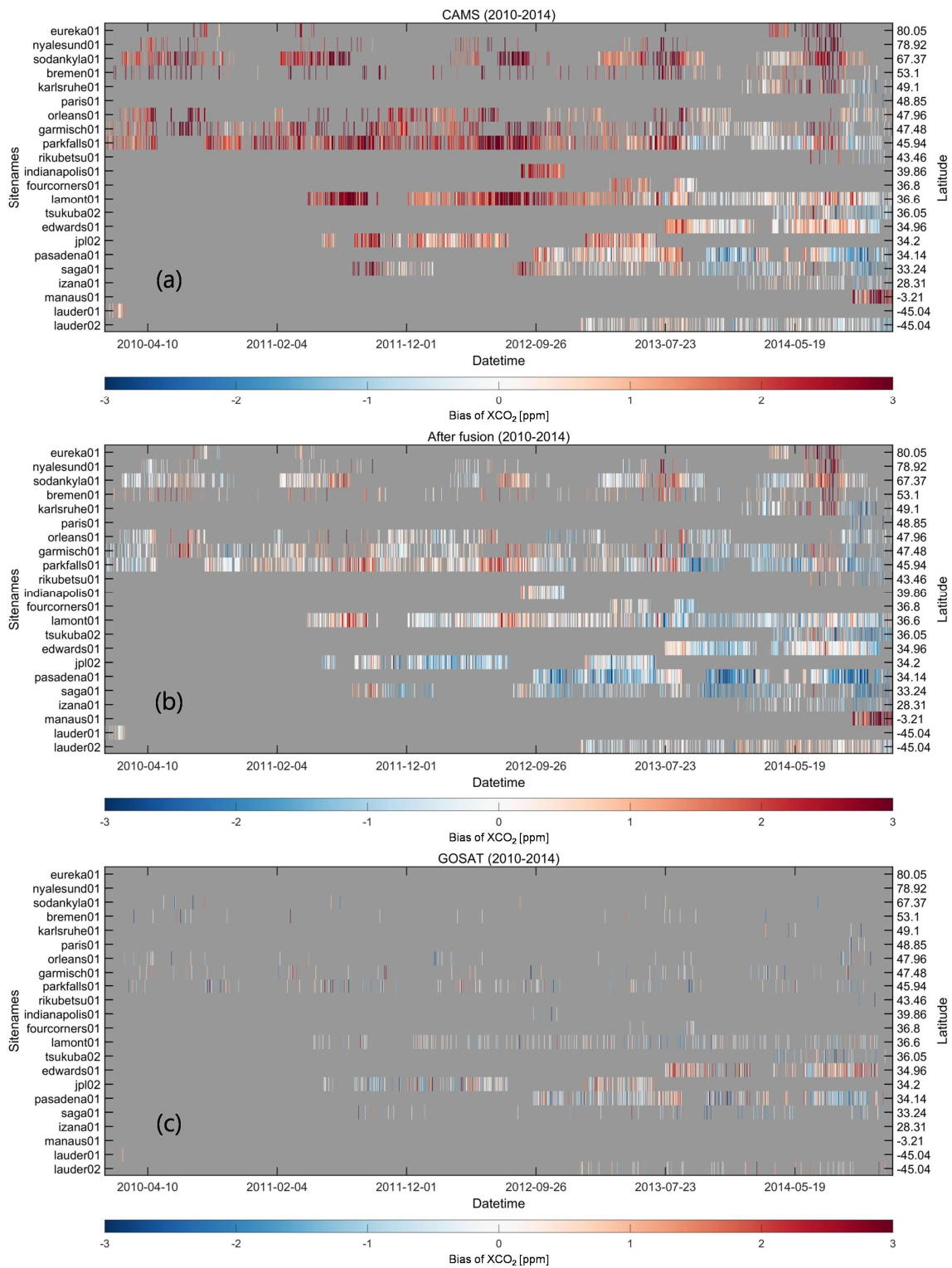
Figure 8. Heat maps of the biases between daily (a) CAMS-EGG4/(b) fused/(c) GOSAT and TCCON XCO$_2$ over time and latitude. Color ramps stand for the biases of XCO$_2$. Background colors (grey) indicate the missing data.

Figure 9. Heat maps of the biases between daily (a) CAMS-EGG4/(b) fused/(c) OCO-2 and TCCON XCO₂ over time and latitude. Color ramps stand for the biases of XCO₂. Background colors (grey) indicate the missing data.
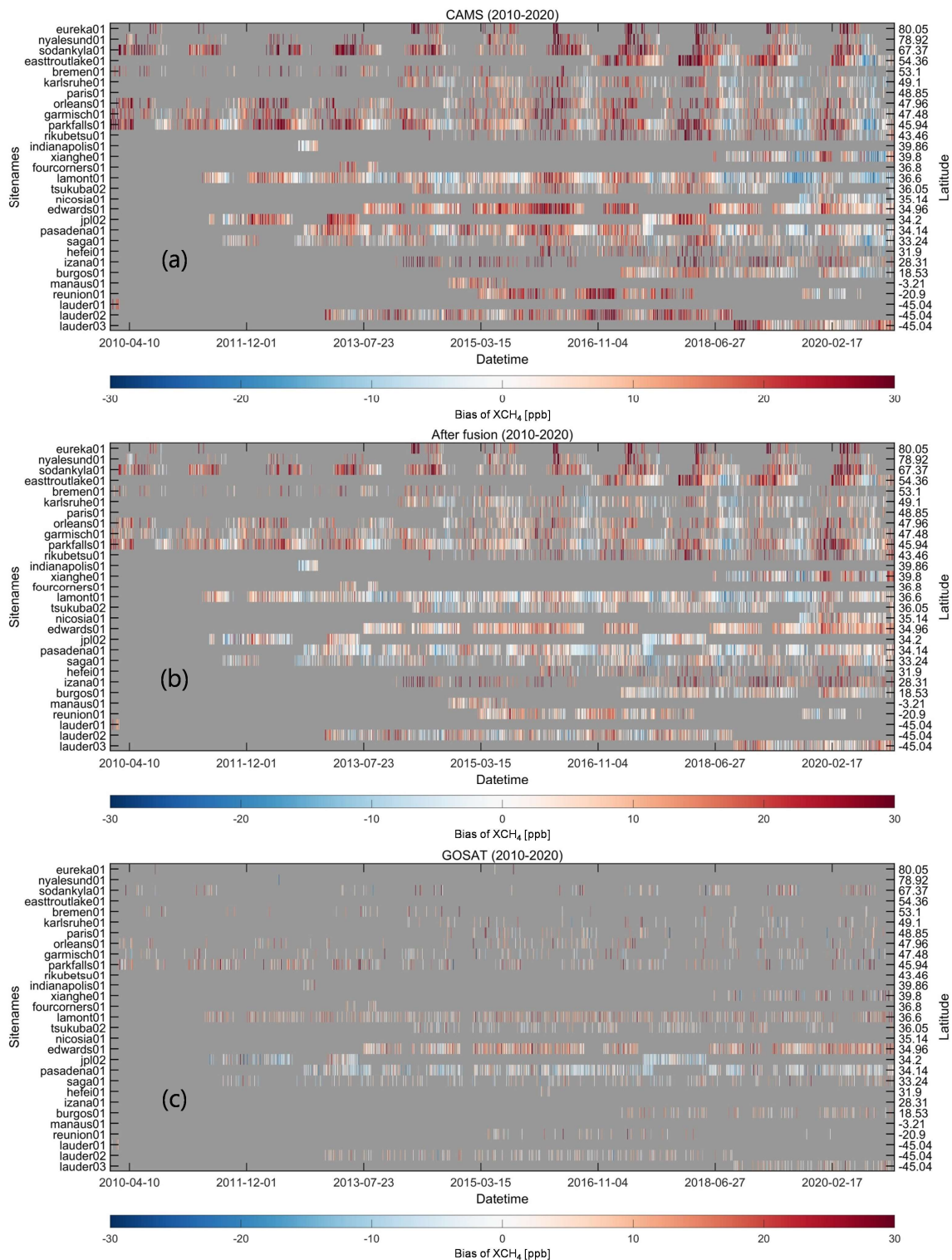
Figure 10. Heat maps of the biases between daily (a) CAMS-EGG4/(b) fused/(c) GOSAT and TCCON XCH$_4$ over time and latitude. Color ramps stand for the biases of XCO$_2$. Background colors (grey) indicate the missing data.

Figure 6 and 7 demonstrate the time series for daily CAMS-EGG4, GOSAT, OCO-2, fused, and TCCON data on individual in-situ stations. Similarly, two stations, i.e., garmisch01 and lauder02, are regarded as examples, which locate in Europe and Oceania, respectively. As depicted in Fig. 6, the XCO$_2$ from CAMS-EGG4 is markedly overestimated on garmisch01 from 2010 to 2014 and in 2020. After fusion, the XCO$_2$ presents an equal trend compared to TCCON measurements over time, with smaller μ (0.096 and 0.139 ppm) and σ (1.067 and 1.01 ppm). In the meantime, the overestimation of CAMS-EGG4 XCH$_4$

288 is also mitigated on garmisch01 through our fusion method. Regarding lauder02, Figure 7 shows that CAMS-EGG4 generates

289 underestimated XCO_2 (2015-2019) and overestimated XCH_4. The μ and σ of the fused results (e.g., 4.952 and 10.189 ppb

290 for XCH_4) are significantly improved on lauder02.
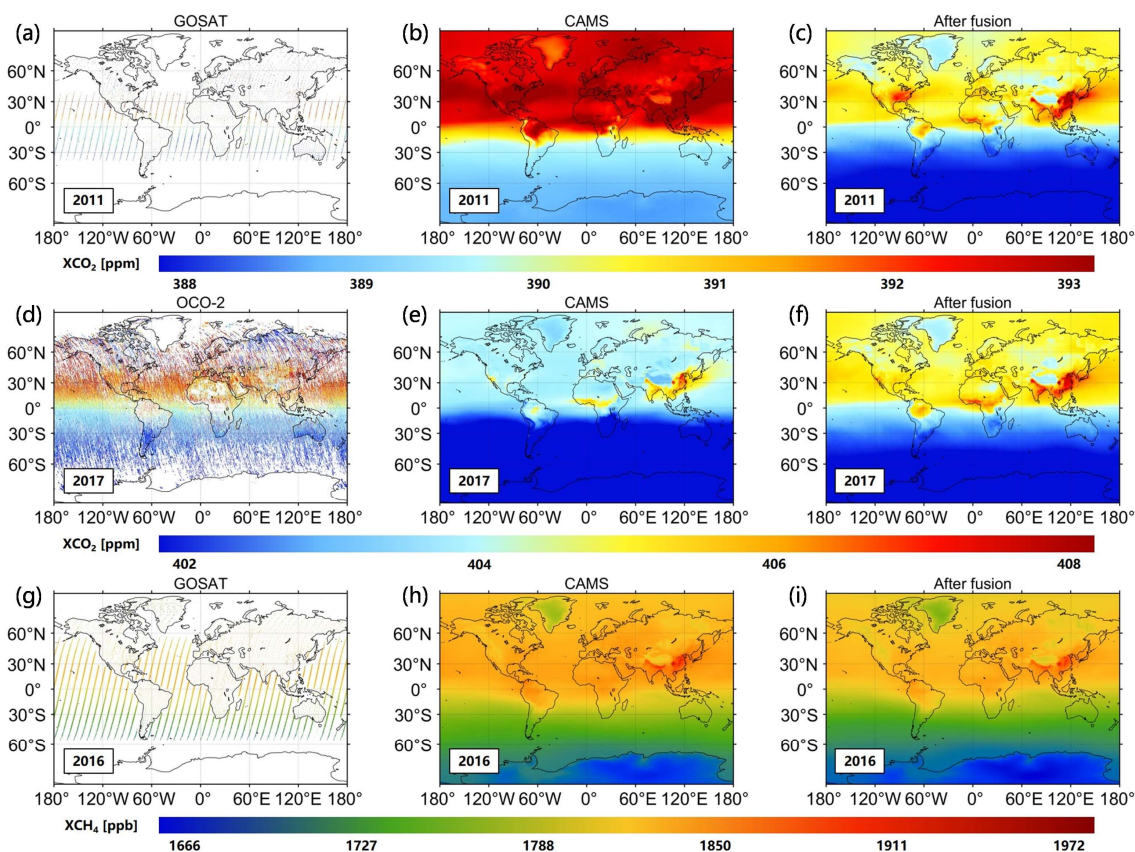
291

292 **Figure 11.** Annual (a and g) GOSAT, (d) OCO-2, (b, e, and h) CAMS-EGG4, and (c, f, and i) fused XCO_2/XCH_4 over the globe. Color

293 ramps stand for the values of XCO_2 and XCH_4.

4.3 Uncertainty analyses

295 Figure 8-10 display the biases between daily CAMS-EGG4/fused/GOSAT/OCO-2 and TCCON data over time and latitude.

296 As observed in Fig. 8 and 9, a large overestimation generally exists in the CAMS-EGG4 XCO_2 from 2010 to 2014 and in 2020,

297 especially before 2013 and in 2020 (> 3 ppm). These are attributed to the considerable errors in the satellite data assimilated

298 (2010-2014) and that anthropogenic emissions are not modified for COVID-19 lockdowns in 2020 (Agusti-Panareda et al.,

299 2022). After fusion, the biases of XCO_2 are well improved for most TCCON in-situ stations from 2010 to 2014 and in 2020,

300 whose patterns are similar to those of GOSAT and OCO-2 XCO_2, respectively. This indicates that the proposed fusion method

301 can effectively correct the biases in CAMS-EGG4 due to the issues from assimilation data. Meanwhile, CAMS-EGG4

302 generates distinctly underestimated XCO_2 from 2016 to 2019 on the stations of latitude < 40° N, which is also mitigated via

303 the S-STDCT fusion method (see Fig. 10). Moreover, the CAMS-EGG4 XCH_4 frequently presents a large positive bias (> 30

304 ppb), while the fused XCH_4 only enhances the performance on the stations of latitude < 50° N. The improvements for other

305 stations require our further efforts in the future.

306
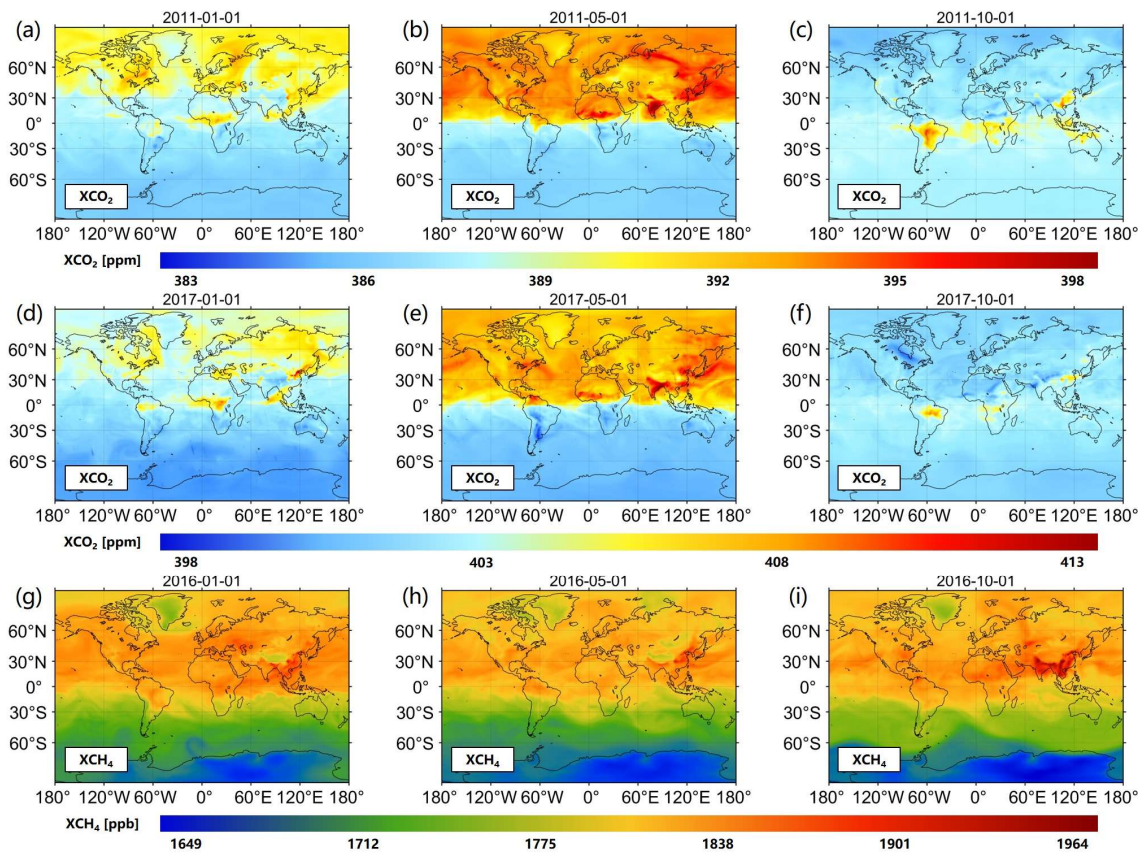
Figure 12. Daily fused (a-f) XCO₂ and (g-i) XCH₄ over the globe. Color ramps stand for the values of XCO₂ and XCH₄.

308
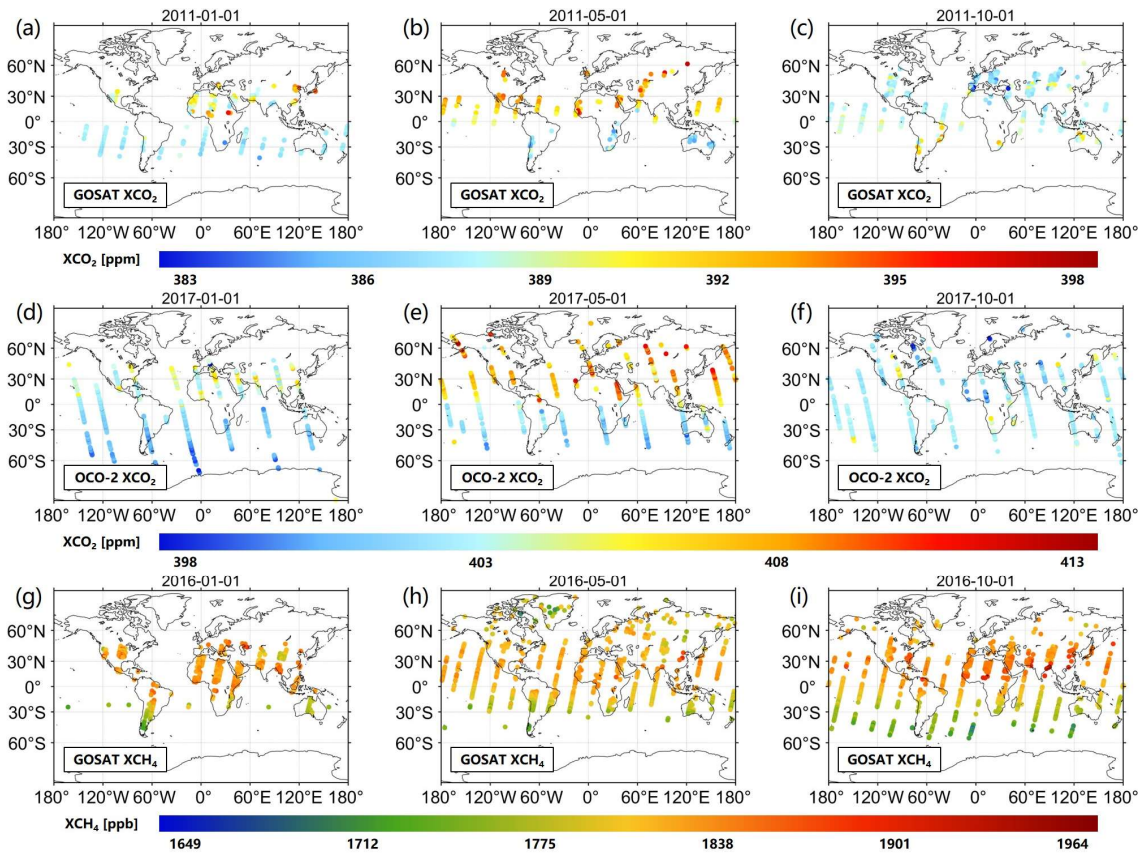
Figure 13. Daily (a-c) GOSAT, (d-f) OCO-2 XCO₂, and (g-i) GOSAT XCH₄ over the globe. Color ramps stand for the values of XCO₂ and XCH₄.

4.4 Assessment of spatial distribution on multi-temporal scales

Figure 11 demonstrates the comparisons of annual GOSAT, OCO-2, CAMS-EGG4, and fused XCO_2/XCH_4 over the globe. A total of three years are selected, including 2011, 2017, and 2016. As can be seen, the fused results present coincident spatial patterns with GOSAT and OCO-2, even if the annual GOSAT and OCO-2 data are greatly sparse. Particularly, the large overestimation and underestimation of CAMS-EGG4 XCO_2 in 2011 and 2017 are significantly modified after fusion, respectively, which are mutually confirmed with the descriptions in Section 4.3.

Figure 12 illustrates the examples of daily fused XCO_2 and XCH_4 over the globe, consisting of three days in three years. As shown, the fused results display detailed information on atmospheric CO_2 and CH_4, which clearly indicate their regional and global spatial patterns. In addition, incoherent or factitious spatial distribution is not observed in the fused XCO_2 and XCH_4. Next, Fig. 13 provides the corresponding daily XCO_2 and XCH_4 from GOSAT and OCO-2 over the globe. It is worth noting that the daily satellite XCO_2 and XCH_4 are mapped via footprints due to their significant sparse coverage, which are nearly invisible at grids of 0.25°. As expected, the fused results present identical spatial distribution compared to XCO_2 and XCH_4 from GOSAT and OCO-2. This suggests the robustness and reliability of the proposed fusion method.

Figure 14 depicts the multi-year mean fused global XCO_2 and XCH_4 from 2010 to 2020. Generally, the spatial patterns of XCO_2 and XCH_4 are divided by the equator. The high values of XCO_2 and XCH_4 mainly distribute over Asia, e.g., China and India, which is attributed to the large anthropogenic emissions (Kenea et al., 2023; Liu et al., 2020; Turner et al., 2015; Hotchkiss et al., 2015). In the meantime, considerable natural emissions, e.g., wildfires (Arora and Melton, 2018), also can obviously increase the XCO_2 values, such as in central Africa and northern South America. Figure 15 and 16 illustrate the seasonal fused XCO_2 and XCH_4 from 2010 to 2020 over the globe, respectively. As displayed, seasonal changes of global XCO_2 and XCH_4 spatial patterns are clearly reflected in the fused results. Compared to XCH_4, the global spatial patterns of XCO_2 vary more drastically. This is likely driven by the spatiotemporal heterogeneity of meteorological fields (Liu et al., 2011) and different emission sources of CO_2 and CH_4.
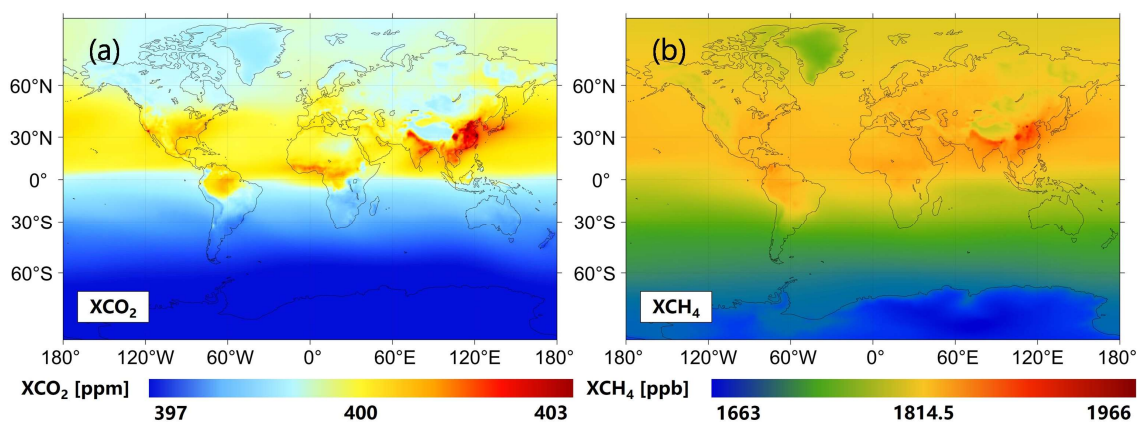
Figure 14. Multi-year mean fused (a) XCO_2 and (b) XCH_4 from 2010 to 2020 over the globe. Color ramps stand for the values of XCO_2 and XCH_4.

336
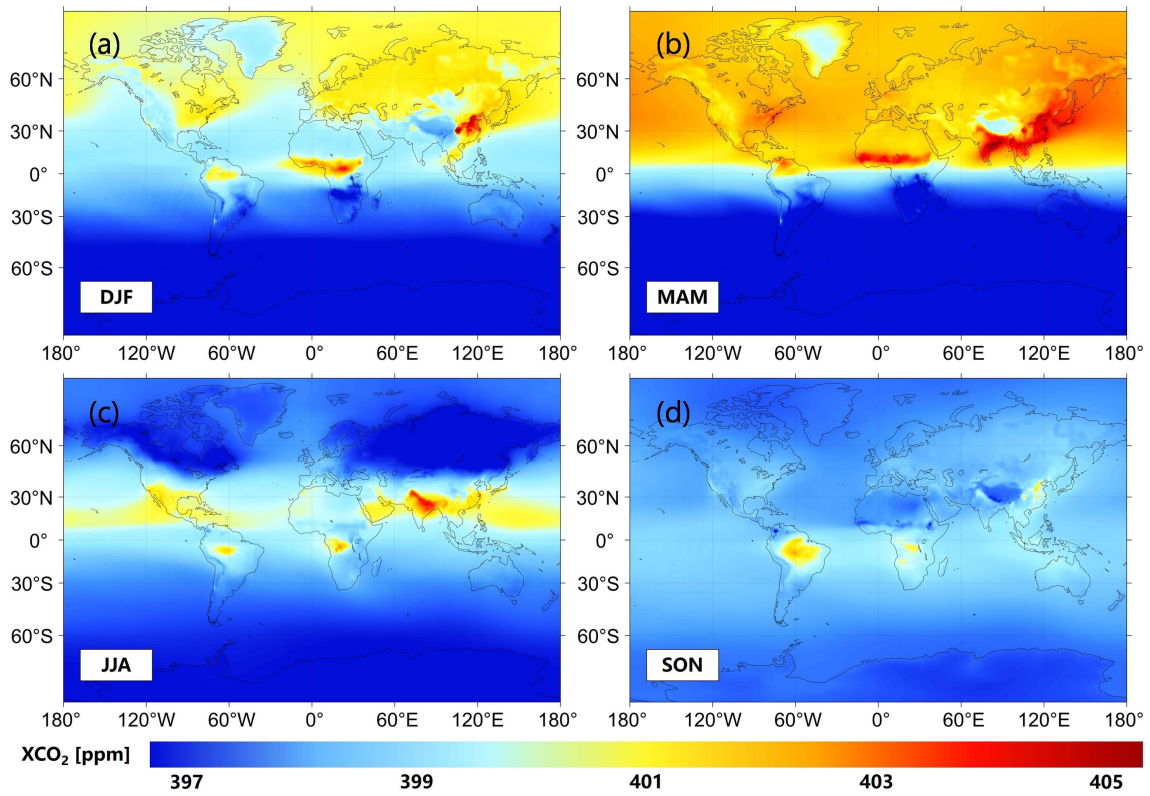
Figure 15. Seasonal fused XCO₂ from 2010 to 2020 over the globe. The color ramp stands for the value of XCO2. (a) DJF, (b) MAM, (c) JJA, and (d) SON denote Dec. to Feb., Mar. to May., Jun. to Aug., and Sep. to Nov., respectively.

339
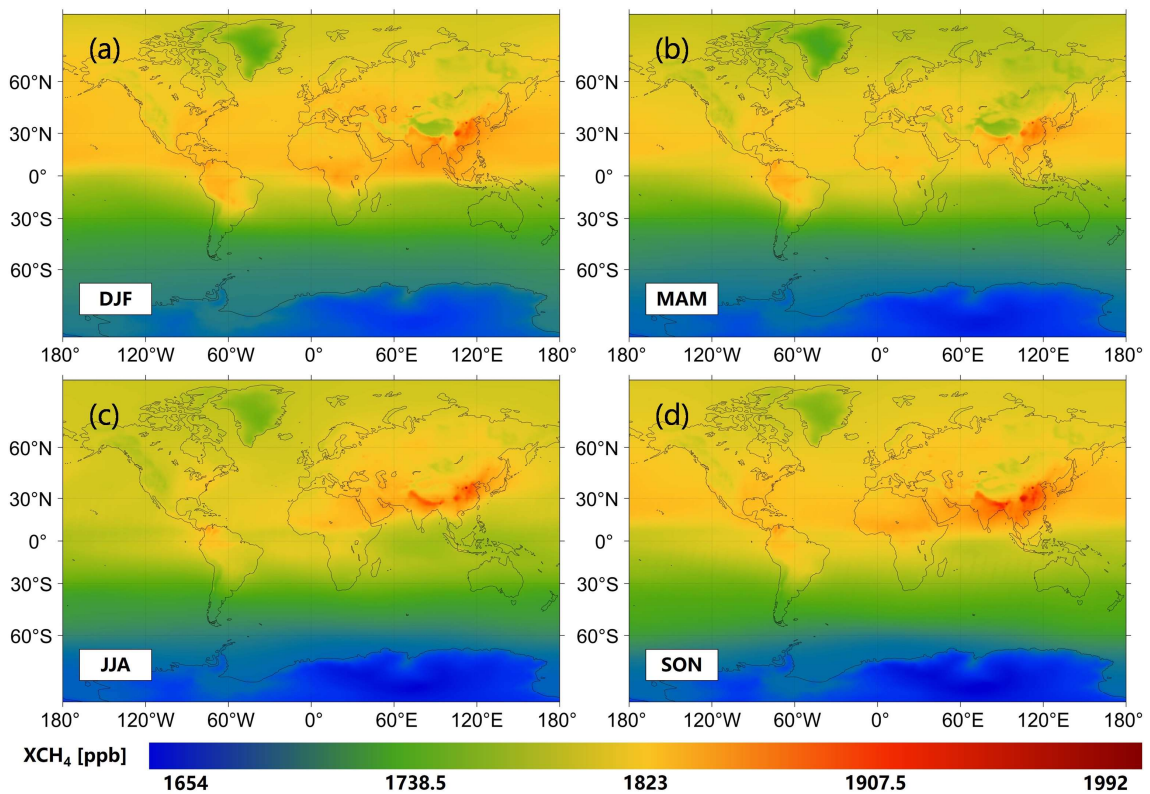
Figure 16. Seasonal fused XCH4 from 2010 to 2020 over the globe. The color ramp stands for the value of XCH4. (a) DJF, (b) MAM, (c) JJA, and (d) SON denote Dec. to Feb., Mar. to May., Jun. to Aug., and Sep. to Nov., respectively.

342 Figure 17 and 18 map the annual fused global XCO₂ and XCH₄ from 2010 to 2020, respectively, including their trends. As

343 observed in Fig. 17, the CO_2 levels continuously increase from 2010 to 2020, with the mean XCO_2 values ranging from $\leq$

344 386 to $\geq$ 416 ppm. However, the trends of XCO_2 only present small spatial differences (~ 0.2 ppm per year), of which the

345 large growth rates primally distribute along the equator, especially for China ($\geq$ 2.5 ppm per year). It is worth noting that the

346 growth rates of XCO_2 are relatively slight ($\leq$ 2.3 ppm per year) in northern South America compared to other regions. This is

347 likely caused by the effects from the carbon sequestration of forests (Chazdon et al., 2016). Besides, the XCH_4 values also

348 notably rise from 2010 to 2020, of which the maximum is not less than 2008 ppb in 2020 (see Fig. 18). The large growth rates

349 of XCH_4 are majorly discovered over southern Asia and northern Europe.

350 **5 Data availability**

351 The fused results can be freely accessed at http://doi.org/10.5281/zenodo.7388893 (Wang et al., 2022b). The daily global

352 seamless gridded (0.25°) XCO_2 and XCH_4 from 2010 to 2020 are stored in the netCDF4 format with a file size of ~ 3.5 MB

353 for each day. The units of XCO_2 and XCH_4 are ppm and ppb, respectively.
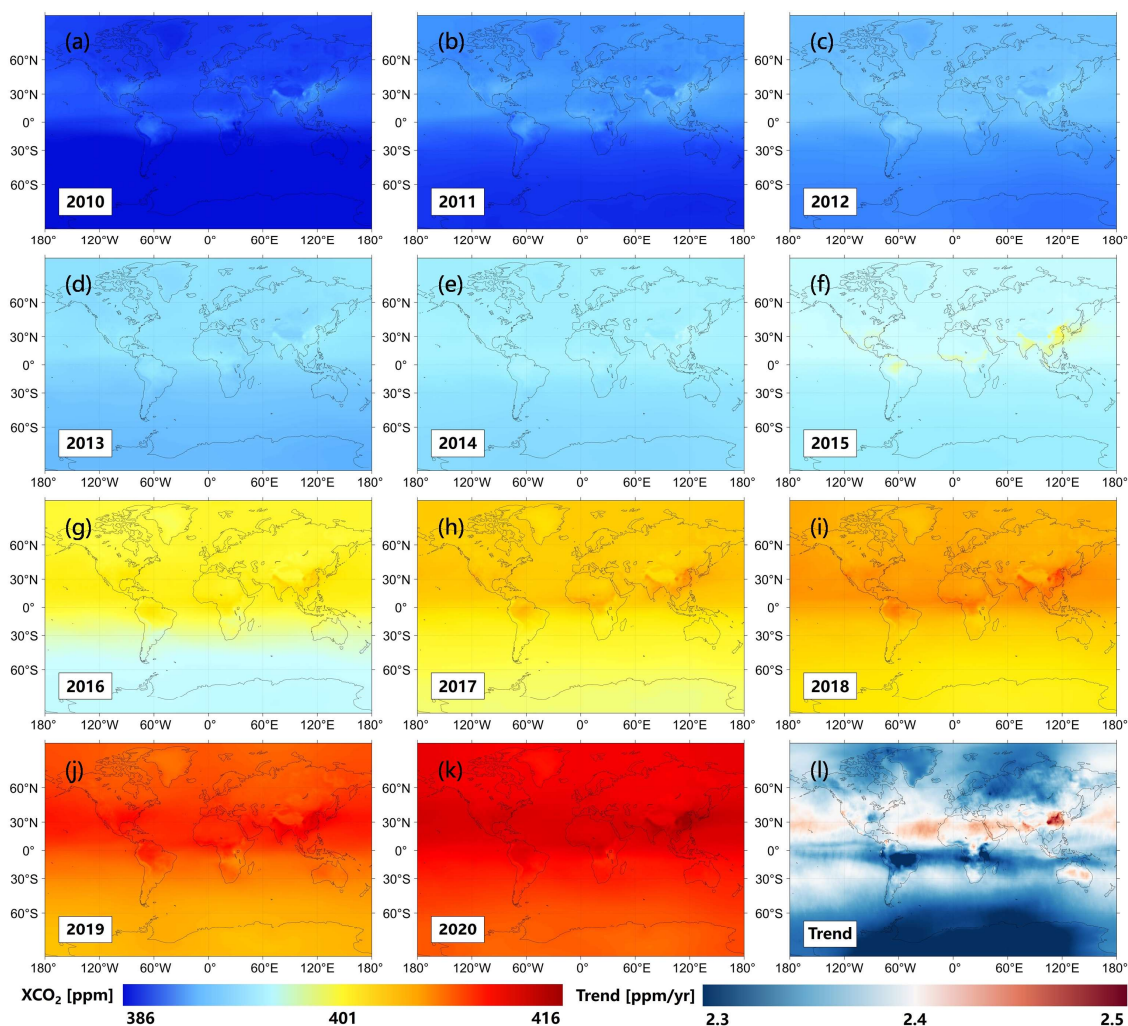
354
355 **Figure 17.** Annual fused (a-k) XCO_2 and (l) its trend from 2010 to 2020 over the globe. Color ramps stand for the values of XCO_2 and its
356 trend. ppm/yr: ppm per year.

357

6 Conclusions

In our study, a novel spatiotemporally self-supervised fusion method, i.e., S-STDCT, is proposed to acquire long-term daily seamless globally distributed XCO_2 and XCH_4 products from 2010 to 2020 at the grids of 0.25°. A total of three datasets are adopted, which include GOSAT, OCO-2, and CAMS-EGG4. Since the data from GOSAT and OCO-2 is greatly sparse in space-time domain, the algorithm for frequency domain (the *STDCT*) is applied in the fusion task. Validation results show that the S-STDCT fusion method performs well over the globe, with the σ of ~ 1.18 ppm for XCO_2 and 11.3 ppb for XCH_4 against TCCON measurements during 2010-2020. Meanwhile, the R^2 of fused XCO_2 and XCH_4 reach 0.91/0.95 (2010-2014/2015-2020) and 0.9 (2010-2020), respectively. Generally, the accuracy of fused results is distinctly superior to that of CAMS-EGG4, which also exceeds or equals those of GSOAT and OCO-2. Particularly, the proposed fusion method effectively modifies the large biases in CAMS-EGG4 caused by the issues from assimilation data, such as the uncorrected anthropogenic emission inventories for COVID-19 lockdowns in 2020. Besides, the spatial patterns of fused results remain coincident with GOSAT and OCO-2, which can accurately display the long-term and seasonal changes of global XCO_2 and XCH_4 spatial distribution.

The long-term (2010-2020) daily global seamless gridded (0.25°) fused results are available at http://doi.org/10.5281/zenodo.7388893 (Wang et al., 2022b).

Overall, the developed fusion method generates high-quality full-coverage XCO_2 and XCH_4 datasets over the globe from 2010 to 2020. However, it only considers the global spatiotemporal knowledge of self-correlation in GOSAT and OCO-2 products without attention to local spatiotemporal information. Meanwhile, the spatial resolution and available period of fused results should be further enhanced, which are devised as 0.1° and more than 20 years (e.g., 2000-2020), respectively. To fix these issues, we will spare no effort to work on our future works.

Author contributions

YW designed the study, collected and processed the data, analyzed the results, and wrote the paper. QQY and TWL provided constructive comments on the paper. YJY, SQZ, and LPZ revised the paper. All authors contributed to the study.

Competing interests

The contact author has declared that none of the authors has any competing interests.

Disclaimer

Publisher's note: Copernicus Publications remains neutral with regard to jurisdictional claims in published maps and institutional affiliations.

Acknowledgments

The authors would like to express gratitude to the Goddard Earth Science Data and Information Services Center for providing the GOSAT and OCO-2 XCO_2 products (last access: 20 November 2022 and 27 November 2022), the Centre for Environmental Data Analysis for providing the GOSAT XCH_4 product (last access: 18 November 2022), the Copernicus Climate Data Store for providing the CAMS-EGG4 XCO_2 and XCH_4 products (last access: 25 November 2022), the Total Carbon Column Observing Network (hosted by CaltechDATA at https://tccondata.org; Chair: Dr. Debra Wunch) for establishing and maintaining in-situ stations (last access: 18 November 2022).

Financial support

Our work is supported by the National Natural Science Foundation of China (No. 41922008), the Basic and Applied Basic Research Foundation of Guangdong Province (No. 2021A1515110567), and the Hubei Science Foundation for Distinguished

397 Young Scholars (No. 2020CFA051).

398 **References**

399 Agusti-Panareda, A., Barré, J., Massart, S., Inness, A., Aben, I., Ades, M., Baier, B. C., Balsamo, G., Borsdorff, T.,
400 Bousserez, N., Boussetta, S., Buchwitz, M., Cantarello, L., Crevoisier, C., Engelen, R., Eskes, H., Flemming, J.,
401 Garrigues, S., Hasekamp, O., Huijnen, V., Jones, L., Kipling, Z., Langerock, B., McNorton, J., Meilhac, N., Noel, S.,
402 Parrington, M., Peuch, V.-H., Ramonet, M., Ratzinger, M., Reuter, M., Ribas, R., Suttie, M., Sweeney, C., Tarniewicz,
403 J., and Wu, L.: Technical note: The CAMS greenhouse gas reanalysis from 2003 to 2020, EGUsphere, 1–51,
404 https://doi.org/10.5194/egusphere-2022-283, 2022.

405 Arora, V. K. and Melton, J. R.: Reduction in global area burned and wildfire emissions since 1930s enhances carbon
406 uptake by land, Nat Commun, 9, 1326, https://doi.org/10.1038/s41467-018-03838-0, 2018.

407 August, T., Klaes, D., Schlüssel, P., Hultberg, T., Crapeau, M., Arriaga, A., O'Carroll, A., Coppens, D., Munro, R., and
408 Calbet, X.: IASI on Metop-A: Operational Level 2 retrievals after five years in orbit, Journal of Quantitative
409 Spectroscopy and Radiative Transfer, 113, 1340–1371, https://doi.org/10.1016/j.jqsrt.2012.02.028, 2012.

410 Battin, T. J., Luyssaert, S., Kaplan, L. A., Aufdenkampe, A. K., Richter, A., and Tranvik, L. J.: The boundless carbon
411 cycle, Nature Geosci, 2, 598–600, https://doi.org/10.1038/ngeo618, 2009.

412 Beirle, S., Lampel, J., Wang, Y., Mies, K., Dörner, S., Grossi, M., Loyola, D., Dehn, A., Danielczok, A., Schröder, M.,
413 and Wagner, T.: The ESA GOME-Evolution "Climate" water vapor product: a homogenized time series of H_2O columns
414 from GOME, SCIAMACHY, and GOME-2, Earth System Science Data, 10, 449–468, https://doi.org/10.5194/essd-10-
415 449-2018, 2018.

416 Bergamaschi, P., Houweling, S., Segers, A., Krol, M., Frankenberg, C., Scheepmaker, R. A., Dlugokencky, E., Wofsy, S.
417 C., Kort, E. A., Sweeney, C., Schuck, T., Brenninkmeijer, C., Chen, H., Beck, V., and Gerbig, C.: Atmospheric CH_4 in
418 the first decade of the 21st century: Inverse modeling analysis using SCIAMACHY satellite retrievals and NOAA surface
419 measurements, Journal of Geophysical Research: Atmospheres, 118, 7350–7369, https://doi.org/10.1002/jgrd.50480,
420 2013.

421 Bhattacharjee, S., Mitra, P., and Ghosh, S. K.: Spatial Interpolation to Predict Missing Attributes in GIS Using Semantic
422 Kriging, IEEE Transactions on Geoscience and Remote Sensing, 52, 4771–4780,
423 https://doi.org/10.1109/TGRS.2013.2284489, 2014.

424 Buchwitz, M., Reuter, M., Schneising, O., Boesch, H., Guerlet, S., Dils, B., Aben, I., Armante, R., Bergamaschi, P.,
425 Blumenstock, T., Bovensmann, H., Brunner, D., Buchmann, B., Burrows, J. P., Butz, A., Chédin, A., Chevallier, F.,
426 Crevoisier, C. D., Deutscher, N. M., Frankenberg, C., Hase, F., Hasekamp, O. P., Heymann, J., Kaminski, T., Laeng, A.,
427 Lichtenberg, G., De Mazière, M., Noël, S., Notholt, J., Orphal, J., Popp, C., Parker, R., Scholze, M., Sussmann, R., Stiller,
428 G. P., Warneke, T., Zehner, C., Bril, A., Crisp, D., Griffith, D. W. T., Kuze, A., O'Dell, C., Oshchepkov, S., Sherlock, V.,
429 Suto, H., Wennberg, P., Wunch, D., Yokota, T., and Yoshida, Y.: The Greenhouse Gas Climate Change Initiative (GHG-
430 CCI): Comparison and quality assessment of near-surface-sensitive satellite-derived CO_2 and CH_4 global data sets,
431 Remote Sensing of Environment, 162, 344–362, https://doi.org/10.1016/j.rse.2013.04.024, 2015.

432 Burrows, J. P., Hölzle, E., Goede, A. P. H., Visser, H., and Fricke, W.: SCIAMACHY—scanning imaging absorption
433 spectrometer for atmospheric chartography, Acta Astronautica, 35, 445–451, https://doi.org/10.1016/0094-
434 5765(94)00278-T, 1995.

Chazdon, R. L., Broadbent, E. N., Rozendaal, D. M. A., Bongers, F., Zambrano, A. M. A., Aide, T. M., Balvanera, P., Becknell, J. M., Boukili, V., Brancalion, P. H. S., Craven, D., Almeida-Cortez, J. S., Cabral, G. A. L., de Jong, B., Denslow, J. S., Dent, D. H., DeWalt, S. J., Dupuy, J. M., Durán, S. M., Espírito-Santo, M. M., Fandino, M. C., César, R. G., Hall, J. S., Hernández-Stefanoni, J. L., Jakovac, C. C., Junqueira, A. B., Kennard, D., Letcher, S. G., Lohbeck, M., Martínez-Ramos, M., Massoca, P., Meave, J. A., Mesquita, R., Mora, F., Muñoz, R., Muscarella, R., Nunes, Y. R. F., Ochoa-Gaona, S., Orihuela-Belmonte, E., Peña-Claros, M., Pérez-García, E. A., Piotto, D., Powers, J. S., Rodríguez-Velazquez, J., Romero-Pérez, I. E., Ruíz, J., Saldarriaga, J. G., Sanchez-Azofeifa, A., Schwartz, N. B., Steininger, M. K., Swenson, N. G., Uriarte, M., van Breugel, M., van der Wal, H., Veloso, M. D. M., Vester, H., Vieira, I. C. G., Bentos, T. V., Williamson, G. B., and Poorter, L.: Carbon sequestration potential of second-growth forest regeneration in the Latin American tropics, Science Advances, 2, e1501639, https://doi.org/10.1126/sciadv.1501639, 2016.

Chen, H., Xu, X., Fang, C., Li, B., and Nie, M.: Differences in the temperature dependence of wetland CO_2 and CH_4 emissions vary with water table depth, Nat. Clim. Chang., 11, 766–771, https://doi.org/10.1038/s41558-021-01108-4, 2021.

Choulga, M., Janssens-Maenhout, G., Super, I., Solazzo, E., Agusti-Panareda, A., Balsamo, G., Bousserez, N., Crippa, M., Denier van der Gon, H., Engelen, R., Guizzardi, D., Kuenen, J., McNorton, J., Oreggioni, G., and Visschedijk, A.: Global anthropogenic CO_2 emissions and uncertainties as a prior for Earth system modelling and data assimilation, Earth System Science Data, 13, 5311–5335, https://doi.org/10.5194/essd-13-5311-2021, 2021.

Cintra, R. J. and Bayer, F. M.: A DCT Approximation for Image Compression, IEEE Signal Processing Letters, 18, 579–582, https://doi.org/10.1109/LSP.2011.2163394, 2011.

Crisp, D., Pollock, H. R., Rosenberg, R., Chapsky, L., Lee, R. A. M., Oyafuso, F. A., Frankenberg, C., O'Dell, C. W., Bruegge, C. J., Doran, G. B., Eldering, A., Fisher, B. M., Fu, D., Gunson, M. R., Mandrake, L., Osterman, G. B., Schwandner, F. M., Sun, K., Taylor, T. E., Wennberg, P. O., and Wunch, D.: The on-orbit performance of the Orbiting Carbon Observatory-2 (OCO-2) instrument and its radiometrically calibrated products, Atmospheric Measurement Techniques, 10, 59–81, https://doi.org/10.5194/amt-10-59-2017, 2017.

Crosswell, J. R., Anderson, I. C., Stanhope, J. W., Van Dam, B., Brush, M. J., Ensign, S., Piehler, M. F., McKee, B., Bost, M., and Paerl, H. W.: Carbon budget of a shallow, lagoonal estuary: Transformations and source-sink dynamics along the river-estuary-ocean continuum, Limnology and Oceanography, 62, S29–S45, https://doi.org/10.1002/lno.10631, 2017.

Deng, F., Jones, D. B. A., Henze, D. K., Bousserez, N., Bowman, K. W., Fisher, J. B., Nassar, R., O'Dell, C., Wunch, D., Wennberg, P. O., Kort, E. A., Wofsy, S. C., Blumenstock, T., Deutscher, N. M., Griffith, D. W. T., Hase, F., Heikkinen, P., Sherlock, V., Strong, K., Sussmann, R., and Warneke, T.: Inferring regional sources and sinks of atmospheric CO_2 from GOSAT XCO_2 data, Atmospheric Chemistry and Physics, 14, 3703–3727, https://doi.org/10.5194/acp-14-3703-2014, 2014.

Doughty, R., Kurosu, T. P., Parazoo, N., Köhler, P., Wang, Y., Sun, Y., and Frankenberg, C.: Global GOSAT, OCO-2, and OCO-3 solar-induced chlorophyll fluorescence datasets, Earth System Science Data, 14, 1513–1529, https://doi.org/10.5194/essd-14-1513-2022, 2022.

El-Mahallawy, M. S. and Hashim, M.: Material Classification of Underground Utilities From GPR Images Using DCT-Based SVM Approach, IEEE Geoscience and Remote Sensing Letters, 10, 1542–1546, https://doi.org/10.1109/LGRS.2013.2261796, 2013.

Fraser, A., Palmer, P. I., Feng, L., Boesch, H., Cogan, A., Parker, R., Dlugokencky, E. J., Fraser, P. J., Krummel, P. B.,

Langenfelds, R. L., O'Doherty, S., Prinn, R. G., Steele, L. P., van der Schoot, M., and Weiss, R. F.: Estimating regional methane surface fluxes: the relative importance of surface and GOSAT mole fraction measurements, Atmospheric Chemistry and Physics, 13, 5697–5713, https://doi.org/10.5194/acp-13-5697-2013, 2013.

Fredj, E., Roarty, H., Kohut, J., Smith, M., and Glenn, S.: Gap Filling of the Coastal Ocean Surface Currents from HFR Data: Application to the Mid-Atlantic Bight HFR Network, Journal of Atmospheric and Oceanic Technology, 33, 1097–1111, https://doi.org/10.1175/JTECH-D-15-0056.1, 2016.

Garcia, D.: Robust smoothing of gridded data in one and higher dimensions with missing values, Computational Statistics & Data Analysis, 54, 1167–1178, https://doi.org/10.1016/j.csda.2009.09.020, 2010.

Hakkarainen, J., Ialongo, I., and Tamminen, J.: Direct space-based observations of anthropogenic CO_2 emission areas from OCO-2, Geophysical Research Letters, 43, 11,400-11,406, https://doi.org/10.1002/2016GL070885, 2016.

Hamazaki, T., Kaneko, Y., Kuze, A., and Kondo, K.: Fourier transform spectrometer for Greenhouse Gases Observing Satellite (GOSAT), in: Enabling Sensor and Platform Technologies for Spaceborne Remote Sensing, Enabling Sensor and Platform Technologies for Spaceborne Remote Sensing, 73–80, https://doi.org/10.1117/12.581198, 2005.

He, C., Ji, M., Grieneisen, M. L., and Zhan, Y.: A review of datasets and methods for deriving spatiotemporal distributions of atmospheric CO_2, Journal of Environmental Management, 322, 116101, https://doi.org/10.1016/j.jenvman.2022.116101, 2022a.

He, C., Ji, M., Li, T., Liu, X., Tang, D., Zhang, S., Luo, Y., Grieneisen, M. L., Zhou, Z., and Zhan, Y.: Deriving Full-Coverage and Fine-Scale XCO_2 Across China Based on OCO-2 Satellite Retrievals and CarbonTracker Output, Geophysical Research Letters, 49, e2022GL098435, https://doi.org/10.1029/2022GL098435, 2022b.

He, Z., Lei, L., Zhang, Y., Sheng, M., Wu, C., Li, L., Zeng, Z.-C., and Welp, L. R.: Spatio-Temporal Mapping of Multi-Satellite Observed Column Atmospheric CO_2 Using Precision-Weighted Kriging Method, Remote Sensing, 12, 576, https://doi.org/10.3390/rs12030576, 2020.

Hong, X., Zhang, P., Bi, Y., Liu, C., Sun, Y., Wang, W., Chen, Z., Yin, H., Zhang, C., Tian, Y., and Liu, J.: Retrieval of Global Carbon Dioxide From TanSat Satellite and Comprehensive Validation With TCCON Measurements and Satellite Observations, IEEE Transactions on Geoscience and Remote Sensing, 60, 1–16, https://doi.org/10.1109/TGRS.2021.3066623, 2022.

Hotchkiss, E. R., Hall Jr, R. O., Sponseller, R. A., Butman, D., Klaminder, J., Laudon, H., Rosvall, M., and Karlsson, J.: Sources of and processes controlling CO_2 emissions change with the size of streams and rivers, Nature Geosci, 8, 696–699, https://doi.org/10.1038/ngeo2507, 2015.

Houweling, S., Baker, D., Basu, S., Boesch, H., Butz, A., Chevallier, F., Deng, F., Dlugokencky, E. J., Feng, L., Ganshin, A., Hasekamp, O., Jones, D., Maksyutov, S., Marshall, J., Oda, T., O'Dell, C. W., Oshchepkov, S., Palmer, P. I., Peylin, P., Poussi, Z., Reum, F., Takagi, H., Yoshida, Y., and Zhuravlev, R.: An intercomparison of inverse models for estimating sources and sinks of CO_2 using GOSAT measurements, Journal of Geophysical Research: Atmospheres, 120, 5253–5266, https://doi.org/10.1002/2014JD022962, 2015.

Jiang, F., Ju, W., He, W., Wu, M., Wang, H., Wang, J., Jia, M., Feng, S., Zhang, L., and Chen, J. M.: A 10-year global monthly averaged terrestrial net ecosystem exchange dataset inferred from the ACOS GOSAT v9 XCO_2 retrievals (GCAS2021), Earth System Science Data, 14, 3013–3037, https://doi.org/10.5194/essd-14-3013-2022, 2022.

Katzfuss, M. and Cressie, N.: Tutorial on fixed rank kriging (FRK) of CO_2 data, Department of Statistics, The Ohio State

University, Columbus, 2011.

Kenea, S. T., Lee, H., Patra, P. K., Li, S., Labzovskii, L. D., and Joo, S.: Long-term changes in CH_4 emissions: Comparing $\Delta CH_4/\Delta CO_2$ ratios between observation and proved model in East Asia (2010–2020), Atmospheric Environment, 293, 119437, https://doi.org/10.1016/j.atmosenv.2022.119437, 2023.

Kiel, M., O'Dell, C. W., Fisher, B., Eldering, A., Nassar, R., MacDonald, C. G., and Wennberg, P. O.: How bias correction goes wrong: measurement of XCO_2 affected by erroneous surface pressure estimates, Atmospheric Measurement Techniques, 12, 2241–2259, https://doi.org/10.5194/amt-12-2241-2019, 2019.

Laughner, J. L., Roche, S., Kiel, M., Toon, G. C., Wunch, D., Baier, B. C., Biraud, S., Chen, H., Kivi, R., Laemmel, T., McKain, K., Quéhé, P.-Y., Rousogenous, C., Stephens, B. B., Walker, K., and Wennberg, P. O.: A new algorithm to generate a priori trace gas profiles for the GGG2020 retrieval algorithm, Atmospheric Measurement Techniques Discussions, 1–41, https://doi.org/10.5194/amt-2022-267, 2022.

Le Quéré, C., Korsbakken, J. I., Wilson, C., Tosun, J., Andrew, R., Andres, R. J., Canadell, J. G., Jordan, A., Peters, G. P., and van Vuuren, D. P.: Drivers of declining CO_2 emissions in 18 developed economies, Nat. Clim. Chang., 9, 213–217, https://doi.org/10.1038/s41558-019-0419-7, 2019.

Li, L., Lei, L., Song, H., Zeng, Z., and He, Z.: Spatiotemporal Geostatistical Analysis and Global Mapping of CH_4 Columns from GOSAT Observations, Remote Sensing, 14, 654, https://doi.org/10.3390/rs14030654, 2022.

Lin, X., Zhang, W., Crippa, M., Peng, S., Han, P., Zeng, N., Yu, L., and Wang, G.: A comparative study of anthropogenic CH_4 emissions over China based on the ensembles of bottom-up inventories, Earth System Science Data, 13, 1073–1088, https://doi.org/10.5194/essd-13-1073-2021, 2021.

Liu, J., Fung, I., Kalnay, E., and Kang, J.-S.: CO_2 transport uncertainties from the uncertainties in meteorological fields, Geophysical Research Letters, 38, https://doi.org/10.1029/2011GL047213, 2011.

Liu, L. and Greaver, T. L.: A review of nitrogen enrichment effects on three biogenic GHGs: the CO_2 sink may be largely offset by stimulated N_2O and CH_4 emission, Ecology Letters, 12, 1103–1117, https://doi.org/10.1111/j.1461-0248.2009.01351.x, 2009.

Liu, Y., Wang, J., Yao, L., Chen, X., Cai, Z., Yang, D., Yin, Z., Gu, S., Tian, L., Lu, N., and Lyu, D.: The TanSat mission: preliminary global observations, Science Bulletin, 63, 1200–1207, https://doi.org/10.1016/j.scib.2018.08.004, 2018.

Liu, Z., Liu, Z., Song, T., Gao, W., Wang, Y., Wang, L., Hu, B., Xin, J., and Wang, Y.: Long-term variation in CO_2 emissions with implications for the interannual trend in $PM_{2.5}$ over the last decade in Beijing, China, Environmental Pollution, 266, 115014, https://doi.org/10.1016/j.envpol.2020.115014, 2020.

Meinshausen, M., Meinshausen, N., Hare, W., Raper, S. C. B., Frieler, K., Knutti, R., Frame, D. J., and Allen, M. R.: Greenhouse-gas emission targets for limiting global warming to 2 °C, Nature, 458, 1158–1162, https://doi.org/10.1038/nature08017, 2009.

Montzka, S. A., Dlugokencky, E. J., and Butler, J. H.: Non-CO_2 greenhouse gases and climate change, Nature, 476, 43–50, https://doi.org/10.1038/nature10322, 2011.

Moran, D., Pichler, P.-P., Zheng, H., Muri, H., Klenner, J., Kramel, D., Többen, J., Weisz, H., Wiedmann, T., Wyckmans, A., Strømman, A. H., and Gurney, K. R.: Estimating CO_2 emissions for 10000 European cities, Earth System Science Data, 14, 845–864, https://doi.org/10.5194/essd-14-845-2022, 2022.

550 Mueller, T. G., Pusuluri, N. B., Mathias, K. K., Cornelius, P. L., Barnhisel, R. I., and Shearer, S. A.: Map quality for
551 ordinary kriging and inverse distance weighted interpolation, Soil Science Society of America Journal, 68, 2042–2047,
552 2004.

553 Parker, R. J., Webb, A., Boesch, H., Somkuti, P., Barrio Guillo, R., Di Noia, A., Kalaitzi, N., Anand, J. S., Bergamaschi,
554 P., Chevallier, F., Palmer, P. I., Feng, L., Deutscher, N. M., Feist, D. G., Griffith, D. W. T., Hase, F., Kivi, R., Morino, I.,
555 Notholt, J., Oh, Y.-S., Ohyama, H., Petri, C., Pollard, D. F., Roehl, C., Sha, M. K., Shiomi, K., Strong, K., Sussmann, R.,
556 Té, Y., Velazco, V. A., Warneke, T., Wennberg, P. O., and Wunch, D.: A decade of GOSAT Proxy satellite CH_4
557 observations, Earth System Science Data, 12, 3383–3412, https://doi.org/10.5194/essd-12-3383-2020, 2020.

558 Petrescu, A. M. R., Qiu, C., Ciais, P., Thompson, R. L., Peylin, P., McGrath, M. J., Solazzo, E., Janssens-Maenhout, G.,
559 Tubiello, F. N., Bergamaschi, P., Brunner, D., Peters, G. P., Höglund-Isaksson, L., Regnier, P., Lauerwald, R., Bastviken,
560 D., Tsuruta, A., Winiwarter, W., Patra, P. K., Kuhnert, M., Oreggioni, G. D., Crippa, M., Saunois, M., Perugini, L.,
561 Markkanen, T., Aalto, T., Groot Zwaaftink, C. D., Tian, H., Yao, Y., Wilson, C., Conchedda, G., Günther, D., Leip, A.,
562 Smith, P., Haussaire, J.-M., Leppänen, A., Manning, A. J., McNorton, J., Brockmann, P., and Dolman, A. J.: The
563 consolidated European synthesis of CH_4 and N_2O emissions for the European Union and United Kingdom: 1990–2017,
564 Earth System Science Data, 13, 2307–2362, https://doi.org/10.5194/essd-13-2307-2021, 2021.

565 Pham, H. T., Kim, S., Marshall, L., and Johnson, F.: Using 3D robust smoothing to fill land surface temperature gaps at
566 the continental scale, International Journal of Applied Earth Observation and Geoinformation, 82, 101879,
567 https://doi.org/10.1016/j.jag.2019.05.012, 2019.

568 Rao, K. R. and Yip, P.: Discrete Cosine Transform: Algorithms, Advantages, Applications, Academic Press, 517 pp.,
569 2014.

570 Reithmaier, G. M. S., Chen, X., Santos, I. R., Drexl, M. J., Holloway, C., Call, M., Álvarez, P. G., Euler, S., and Maher,
571 D. T.: Rainfall drives rapid shifts in carbon and nutrient source-sink dynamics of an urbanised, mangrove-fringed estuary,
572 Estuarine, Coastal and Shelf Science, 249, 107064, https://doi.org/10.1016/j.ecss.2020.107064, 2021.

573 Shine, K. P., Fuglestvedt, J. S., Hailemariam, K., and Stuber, N.: Alternatives to the Global Warming Potential for
574 Comparing Climate Impacts of Emissions of Greenhouse Gases, Climatic Change, 68, 281–302,
575 https://doi.org/10.1007/s10584-005-1146-9, 2005.

576 Siabi, Z., Falahatkar, S., and Alavi, S. J.: Spatial distribution of XCO_2 using OCO-2 data in growing seasons, Journal of
577 Environmental Management, 244, 110–118, https://doi.org/10.1016/j.jenvman.2019.05.049, 2019.

578 Sjögersten, S., Black, C. R., Evers, S., Hoyos-Santillan, J., Wright, E. L., and Turner, B. L.: Tropical wetlands: A missing
579 link in the global carbon cycle?, Global Biogeochemical Cycles, 28, 1371–1386, https://doi.org/10.1002/2014GB004844,
580 2014.

581 Solomon, S., Daniel, J. S., Sanford, T. J., Murphy, D. M., Plattner, G.-K., Knutti, R., and Friedlingstein, P.: Persistence
582 of climate changes due to a range of greenhouse gases, Proceedings of the National Academy of Sciences, 107, 18354–
583 18359, https://doi.org/10.1073/pnas.1006282107, 2010.

584 Taylor, T. E., O'Dell, C. W., Frankenberg, C., Partain, P. T., Cronk, H. Q., Savtchenko, A., Nelson, R. R., Rosenthal, E.
585 J., Chang, A. Y., Fisher, B., Osterman, G. B., Pollock, R. H., Crisp, D., Eldering, A., and Gunson, M. R.: Orbiting Carbon
586 Observatory-2 (OCO-2) cloud screening algorithms: validation against collocated MODIS and CALIOP data,
587 Atmospheric Measurement Techniques, 9, 973–989, https://doi.org/10.5194/amt-9-973-2016, 2016.

588 Taylor, T. E., O'Dell, C. W., Crisp, D., Kuze, A., Lindqvist, H., Wennberg, P. O., Chatterjee, A., Gunson, M., Eldering,

A., Fisher, B., Kiel, M., Nelson, R. R., Merrelli, A., Osterman, G., Chevallier, F., Palmer, P. I., Feng, L., Deutscher, N. M., Dubey, M. K., Feist, D. G., García, O. E., Griffith, D. W. T., Hase, F., Iraci, L. T., Kivi, R., Liu, C., De Mazière, M., Morino, I., Notholt, J., Oh, Y.-S., Ohyama, H., Pollard, D. F., Rettinger, M., Schneider, M., Roehl, C. M., Sha, M. K., Shiomi, K., Strong, K., Sussmann, R., Té, Y., Velazco, V. A., Vrekoussis, M., Warneke, T., and Wunch, D.: An 11-year record of XCO_2 estimates derived from GOSAT measurements using the NASA ACOS version 9 retrieval algorithm, Earth System Science Data, 14, 325–360, https://doi.org/10.5194/essd-14-325-2022, 2022.

Turner, A. J., Jacob, D. J., Wecht, K. J., Maasakkers, J. D., Lundgren, E., Andrews, A. E., Biraud, S. C., Boesch, H., Bowman, K. W., Deutscher, N. M., Dubey, M. K., Griffith, D. W. T., Hase, F., Kuze, A., Notholt, J., Ohyama, H., Parker, R., Payne, V. H., Sussmann, R., Sweeney, C., Velazco, V. A., Warneke, T., Wennberg, P. O., and Wunch, D.: Estimating global and North American methane emissions with high spatial resolution using GOSAT satellite data, Atmospheric Chemistry and Physics, 15, 7049–7069, https://doi.org/10.5194/acp-15-7049-2015, 2015.

Velazco, V. A., Deutscher, N. M., Morino, I., Uchino, O., Bukosa, B., Ajiro, M., Kamei, A., Jones, N. B., Paton-Walsh, C., and Griffith, D. W. T.: Satellite and ground-based measurements of XCO_2 in a remote semiarid region of Australia, Earth System Science Data, 11, 935–946, https://doi.org/10.5194/essd-11-935-2019, 2019.

Wang, G., Garcia, D., Liu, Y., de Jeu, R., and Johannes Dolman, A.: A three-dimensional gap filling method for large geophysical datasets: Application to global satellite soil moisture observations, Environmental Modelling & Software, 30, 139–142, https://doi.org/10.1016/j.envsoft.2011.10.015, 2012.

Wang, H., Jiang, F., Wang, J., Ju, W., and Chen, J. M.: Terrestrial ecosystem carbon flux estimated using GOSAT and OCO-2 XCO_2 retrievals, Atmospheric Chemistry and Physics, 19, 12067–12082, https://doi.org/10.5194/acp-19-12067-2019, 2019.

Wang, T., Yu, P., Wu, Z., Lu, W., Liu, X., Li, Q. P., and Huang, B.: Revisiting the Intraseasonal Variability of Chlorophyll-a in the Adjacent Luzon Strait With a New Gap-Filled Remote Sensing Data Set, IEEE Transactions on Geoscience and Remote Sensing, 60, 1–11, https://doi.org/10.1109/TGRS.2021.3067646, 2022a.

Wang, Y., Yuan, Q., Li, T., Zhu, L., and Zhang, L.: Estimating daily full-coverage near surface O_3, CO, and NO_2 concentrations at a high spatial resolution over China based on S5P-TROPOMI and GEOS-FP, ISPRS Journal of Photogrammetry and Remote Sensing, 175, 311–325, 2021.

Wang, Y., Yuan, Q., Li, T., and Zhang, L.: Global long-term (2010-2020) daily seamless fused XCO_2 and XCH_4 from CAMS, OCO-2, and GOSAT, https://doi.org/10.5281/zenodo.7388893, 2022b.

Wang, Y., Yuan, Q., Li, T., and Zhu, L.: Global spatiotemporal estimation of daily high-resolution surface carbon monoxide concentrations using Deep Forest, Journal of Cleaner Production, 350, 131500, 2022c.

Wu, L., Hasekamp, O., Hu, H., Landgraf, J., Butz, A., aan de Brugh, J., Aben, I., Pollard, D. F., Griffith, D. W. T., Feist, D. G., Koshelev, D., Hase, F., Toon, G. C., Ohyama, H., Morino, I., Notholt, J., Shiomi, K., Iraci, L., Schneider, M., de Mazière, M., Sussmann, R., Kivi, R., Warneke, T., Goo, T.-Y., and Té, Y.: Carbon dioxide retrieval from OCO-2 satellite observations using the RemoTeC algorithm and validation with TCCON measurements, Atmospheric Measurement Techniques, 11, 3111–3130, https://doi.org/10.5194/amt-11-3111-2018, 2018.

Wunch, D., Toon, G. C., Blavier, J.-F. L., Washenfelder, R. A., Notholt, J., Connor, B. J., Griffith, D. W. T., Sherlock, V., and Wennberg, P. O.: The Total Carbon Column Observing Network, Philosophical Transactions of the Royal Society A: Mathematical, Physical and Engineering Sciences, 369, 2087–2112, https://doi.org/10.1098/rsta.2010.0240, 2011.

Wunch, D., Wennberg, P. O., Osterman, G., Fisher, B., Naylor, B., Roehl, C. M., O'Dell, C., Mandrake, L., Viatte, C.,

Kiel, M., Griffith, D. W. T., Deutscher, N. M., Velazco, V. A., Notholt, J., Warneke, T., Petri, C., De Maziere, M., Sha, M. K., Sussmann, R., Rettinger, M., Pollard, D., Robinson, J., Morino, I., Uchino, O., Hase, F., Blumenstock, T., Feist, D. G., Arnold, S. G., Strong, K., Mendonca, J., Kivi, R., Heikkinen, P., Iraci, L., Podolske, J., Hillyard, P. W., Kawakami, S., Dubey, M. K., Parker, H. A., Sepulveda, E., García, O. E., Te, Y., Jeseck, P., Gunson, M. R., Crisp, D., and Eldering, A.: Comparisons of the Orbiting Carbon Observatory-2 (OCO-2) XCO_2 measurements with TCCON, Atmospheric Measurement Techniques, 10, 2209–2238, https://doi.org/10.5194/amt-10-2209-2017, 2017.

Yoro, K. O. and Daramola, M. O.: Chapter 1 - CO_2 emission sources, greenhouse gases, and the global warming effect, in: Advances in Carbon Capture, edited by: Rahimpour, M. R., Farsi, M., and Makarem, M. A., Woodhead Publishing, 3–28, https://doi.org/10.1016/B978-0-12-819657-1.00001-3, 2020.

Yoshida, Y., Kikuchi, N., Morino, I., Uchino, O., Oshchepkov, S., Bril, A., Saeki, T., Schutgens, N., Toon, G. C., Wunch, D., Roehl, C. M., Wennberg, P. O., Griffith, D. W. T., Deutscher, N. M., Warneke, T., Notholt, J., Robinson, J., Sherlock, V., Connor, B., Rettinger, M., Sussmann, R., Ahonen, P., Heikkinen, P., Kyrö, E., Mendonca, J., Strong, K., Hase, F., Dohe, S., and Yokota, T.: Improvement of the retrieval algorithm for GOSAT SWIR XCO_2 and XCH_4 and their validation using TCCON data, Atmospheric Measurement Techniques, 6, 1533–1547, https://doi.org/10.5194/amt-6-1533-2013, 2013.

Zhang, L., Li, T., and Wu, J.: Deriving gapless CO_2 concentrations using a geographically weighted neural network: China, 2014–2020, International Journal of Applied Earth Observation and Geoinformation, 114, 103063, https://doi.org/10.1016/j.jag.2022.103063, 2022.

Zhang, M. and Liu, G.: Mapping contiguous XCO_2 by machine learning and analyzing the spatio-temporal variation in China from 2003 to 2019, Science of The Total Environment, 858, 159588, https://doi.org/10.1016/j.scitotenv.2022.159588, 2023.

Zhou, S., Wang, Y., Yuan, Q., Yue, L., and Zhang, L.: Spatiotemporal estimation of 6-hour high-resolution precipitation across China based on Himawari-8 using a stacking ensemble machine learning model, Journal of Hydrology, 609, 127718, 2022.